

Optical Characterization and Recovery of
Valuable Matter from Industrial Wastes Towards
Functional Materials

Lukmanul Hakim Arma

Contents

<i>Table Caption</i>	<i>iii</i>
<i>Figure Caption</i>	<i>iv</i>
<i>Acknowledgments</i>	<i>vii</i>

Chapter 1: General Introduction

1.1 Background	2
1.1.1 Pearl oyster farming process and shell waste	4
1.1.2 Rare earth-containing glass-polishing sludge and metallurgical slags	7
1.2 Purpose and construction of this study	11
References	13

Chapter 2: Optical Characterization of Fluorescent Matter in Prismatic Layers of *Pinctada vulgaris* Shell

2.1 Introduction	15
2.2 Experimental methods	18
2.3 Results and discussion	20
2.3.1 Microstructure of prismatic layer	20
2.3.2 Calcitic prismatic layer	20
2.3.3 Thermal decomposition of prismatic layer	22
2.3.4 Excitation and emission spectra of prismatic layer	22
2.3.5 Distribution of fluorescent matter	27
2.3.6 Lamellar pattern of fluorescent matter	33
2.4 Conclusion	39
References	34

**Chapter 3: Rare Earth Recovery from Soda Lime Silicate Glass Cullet
by P₂O₅ Addition**

3.1 Introduction	43
3.2 Experimental methods	46
3.3 Results and discussion	51
3.3.1 Hypersensitive emission spectra to estimate local vicinity of Eu ³⁺ ion . . .	51
3.3.2 Fluorescence intensity ratio of simple glass system	52
3.3.3 Effect of Phosphate addition upon I-ratio of Eu ³⁺ -doped glass cullet	57
3.3.4 The presence of metaphosphate and pyrophosphate groups	60
3.3.5 Recovery of europium	62
3.3.6 Recovery of Eu ³⁺ increases with the presence of metaphosphate chains. . .	64
3.4 Conclusion	64
References	66
Chapter 4: General Conclusion	71

Table Caption

Table 3.1 Phosphate tetrahedral sites in phosphate glass and A/P-ratio.

Table 3.2 Fluorescence intensity ratio of ${}^5D_0 \rightarrow {}^7F_2$ to ${}^5D_0 \rightarrow {}^7F_1$ transition of Eu^{3+} in matrix glasses (silicate, phosphate, phospho-silicate and glass cullet) doped with 1 mol% Eu_2O_3 and quenched in air.

Table 3.3 IR band assignments in the range $500\text{--}1600\text{ cm}^{-1}$ for $(\text{Cullet+Eu})\text{-}x\text{P}_2\text{O}_5$ glass samples doped with 1 mol% Eu_2O_3 and quenched in water.

Figure Caption

Figure 1.1 Pearl oyster farming process and shell waste.

Figure 1.2 Production process of glass showing cullet recycle and generation of glass polishing sludge.

Figure 2.1 A shell of *Pinctada vulgaris* and its cross section showing prismatic layers and nacre layers.

Figure 2.2 Microstructure of calcitic prism (CP) layer. GL is a growth line among parallel growth lines. OM are inter-prismatic organic membranes.

Figure 2.3 X-ray diffraction pattern. (a) CP powdered sample. (b) Calcium carbonate from ICSD powder diffraction file database. Peaks indicate calcite phase.

Figure 2.4 Thermal decomposition of prismatic layer and calcium carbonate reagent. (a) Weight loss of CP powdered sample and CaCO_3 reagent (inset). (b) Five weight losses of CP powdered sample (magnified).

Figure 2.5 Thermal decomposition of prismatic layer and CaCO_3 reagent. (a) Exothermic reaction of CP powdered sample. (b) Exothermic reaction of CaCO_3 reagent.

Figure 2.6 Excitation and emission spectra of as-grinded and heated CP powdered samples.

Figure 2.7 Shell of *Pinctada vulgaris* after being cleaned from oceanic living organism. (a) Outer side of shell shielded by CP layers irradiated by daylight (left side) and commercial UV LED (right side). (b) and (c) Close up of ventral side of shell under daylight and commercial UV LED irradiations, respectively. The circles show areas where the brownish CP layers turn to red whereas pale white unchanged.

Figure 2.8 An inner side of shell (*Pinctada vulgaris*). (a) Inner shell irradiated by commercial UV LED (left side) and daylight (right side). (b) and (c) Area 1 and 2

respectively, that turn to pale blue and red, under commercial UV LED irradiations. Irradiated area size is ~1 mm.

Figure 2.9 Emission spectra of CP powdered sample and inner CP layer. (a) Emission spectrum of CP powdered sample excited at 405 nm. (b) Emission spectrum of inner CP layer on the area 2 in the Figure 2.8(c) excited at 404.7 nm. Detection spot size is ~50 μm .

Figure 2.10 Cross section of shell and CP layers under 404.7 nm irradiation showing lamellar pattern formed by red fluorescence and black lamellae. (a) Nacre as inner side of shell fully covered by the calcitic prism in the outer side. (b) Area 1 on CP layers showing red parallel lines and organic membranes. (c) Area 2 on CP layers. (d) Area 3 on CP layers selected for measuring emission from red and black lamellae. Irradiated area size is ~200 μm –1 mm.

Figure 2.11 Emission spectra of CP powdered and CP thin cross section sample. (a) Emission spectrum of CP powdered sample excited at 405 nm. (b) Emission spectra measured on A, B, C and D spots in lamellar pattern of area 3 as shown in Figure 2.10(d). Red lamellae are the lamellae occupied by organic substance related porphyrin structure. Detection spot size is ~1 μm .

Figure 2.12 Marked area and Elemental mapping on CP layers. (a) Marked area in CP shell sample. The arrows show location of black zone. (b) The marked area, under 404.7 nm irradiation, showing the most black and wider zone between red fluorescent zones. (c) Calcium map of marked area, showing calcium is not concentrated on the black zone. (d) Sulphur map of marked area, showing rich sulphur is concentrated on the black zone than on the adjacent area.

Figure 2.13 Emission spectra of CP powdered and CP thin cross section sample. (a) Emission spectrum of CP powdered sample excited at 405 nm. (b) Emission spectra measured on E, F, and G points in lamellar pattern as shown in Figure 2.12(b). Detection spot size is ~10 μm .

Figure 2.14 Excitation spectra of extracted liquid and CP powdered.

Figure 3.1 Spectra of (cullet+Eu)-35P₂O₅ (1 mol % Eu₂O₃, A/P-ratio = 0.53): (a) excitation spectrum with 614 nm monitored wavelength and (b) emission spectrum with under 393 nm excitation wavelength.

Figure 3.2 Illustration of local structure around Eu³⁺ ion in silicate and phosphate networks: (a) alkali earth or alkaline earth metal (symbolized as A) sits in the second neighbor of Eu³⁺ ion forming Eu-O-A linkage and (b) phosphorus sits in the second neighbor of Eu³⁺ ion forming Eu-O-P linkage.

Figure 3.3 Emission spectra of Eu³⁺ in glass cullet, silicate and phospho-silicate glass matrices under 393 nm excitation: (a) emission intensity at ⁵D₀→⁷F₂ transition for glass cullet+Eu matrix is in comparison to silicate glass, (b) emission intensity at ⁵D₀→⁷F₂ transition for glass cullet+Eu with 45 mol % P₂O₅ addition, (cullet+Eu)-45P₂O₅, is in comparison to phospho-silicate glass matrix. The emission intensity of ⁵D₀→⁷F₁ transition has been normalized to a value of 1.0 to compare visually with that of ⁵D₀→⁷F₂ transition for investigated glasses.

Figure 3.4 Fluorescence intensity ratio of (cullet+Eu)-xP₂O₅ (●) glass samples. Range of intensity ratio for silicate, phosphate, and phospho-silicate glasses from Table 3.2 are pointed by dash lines. Region A: sample composition with A/P-ratio ≤ 1. Region B: sample composition with A/P-ratio > 1. The solid line is guide to the eyes.

Figure 3.5 IR spectra of (cullet+Eu)-xP₂O₅ glass samples. The spectra indicate the presence of pyrophosphate (Q¹) and metaphosphate (Q²) groups. The assignments of absorption band are summarized in Table 3.3.

Figure 3.6 Recovery efficiency of Eu³⁺ dissolved in water in different compositions. Region A: sample composition with A/P- ratio ≤ 1. Region B: sample composition A/P- ratio > 1, also shown in Figure 3.4.

Acknowledgments

I would like to express my sincere gratitude to my advisor, Professor Hiromichi Takebe for his lecture, encouragements, guidance, and invaluable suggestions during my experiments, writing papers and all of my study activities.

I also wish to thank Professor Toshiro Tanaka and Professor Mitsuhiro Okayasu for their valuable lectures. I enjoyed their classes and gained beneficial knowledge and better understanding dealing with physical and mechanical properties of materials.

I would like to extend many thanks to Professor Akira Saitoh and Dr. Satoshi Okano for sharing his knowledge through discussions in any time particularly spectroscopy analysis and introducing experimental apparatus.

I also wish to thank Prof. Tsuyoshi Asahi and Dr. Yukihide Ishibashi for their insight and method of fluorescence microscopy analysis. I wish to thank Professor Masayuki Sakakibara, Dr. Yuri Sueoka, Mr. Idham Andry Kurniawan and all Sakakibara's laboratory members for their assistance of conducting SEM-EDS experiments and ICP-MS sample preparation.

My great appreciation to Takebe's laboratory members: Dr. Shoji Takahashi, Mr. Hoshika Takayuki, Mr. Ryouta Tokunaga, Mr. Hiroki Nakamura, Mr. Arata Tsuruda, Mr. Naoto Kitamura, Mr. Kenta Kuratani and other laboratory's members for their willing cooperation.

I am deeply grateful to Professor Ruth Vergin and Mr. Ozaki Kimiyuki for their invaluable supports during my stay in Matsuyama. I would like to thank management staffs

of Graduate School of Science and Engineering, Ehime University for their sincere help and assistance during my study period. Also, I would like to acknowledge Indonesian government and Hasanuddin University for providing DIKTI-BLN scholarship.

I thank to my friends Dr. Intan Areni and his family, Mr. Irwan Setiawan Muthalib, Dr. Dede Haris Yulianto and his family, Mr. Ady Slamet Riyady and his family, Dr. Ismail Rahim and his family, Mr. Fadhli Syahrial (Malaysian), Dr. Abdul Aziz Ramadhan (Egyptian), Mr. Yousif el-Samani (Sudanese) and all of my friends in Matsuyama for their great supports. Many thanks to Mrs. Namiko Senju and her family for their hospitality to my family, especially providing apartment with very kind neighborhood.

Finally, I wish to dedicate this thesis to my mother, brothers & sisters, my wife Hasriwiani Habo Abbas for all their endless love, supports and prayers, and to my children Imam Fatih Alfathonah, Muh. Rifky Reho Makkiade, Indah Mutiah Utami, Inayah Cintaki, Insyirah Fitrah Ramadhani for all of their inspirations.

Lukmanul Hakim Arma

Optical Characterization and Recovery of Valuable Matter from Industrial Wastes Towards Functional Materials

Lukmanul Hakim Arma

*Department of Materials Science and Biotechnology,
Graduate School of Science and Engineering,
Ehime University*

2016

Chapter 1

General Introduction

1.1 Background

Sustainable development has become a priority for the world since science and technology's impact on the environment has been greatly accelerated in the past century. There is no doubt that science and technology have increased human capacity to extract natural resources through industrial developments, but they have not fully offered parallel and similar insight into how these resources can be returned to their environment or how they could be entered into a new cycle of extraction, processing and use. Many of the resources extracted from nature are used in unsustainable activities and ended up as waste. The waste causes a complex effect on the environment such as, climate change, energy crisis, resource scarcity, and pollution. For these reasons, sustainable development invokes technology to integrate environmental sustainability as its component to be applied in industrial systems. The better it is integrated with the industrial system, the lower the effect on the environment can be.

Several strategies have been introduced to organize environmental components of technology in industries such as zero waste, clean production, and industrial ecology. Zero waste and clean production aim to phase out generation and use of toxic chemicals and materials in the production process by redesigning products and manufacturing methods. In other words, zero waste and clean production look at internal industry improvement to eliminate the inputs of toxic substances into the process chains. Meanwhile, industrial ecology strategy takes a macro level perspective on closing the loop of production flow in inter-industry. Implementation of industrial ecology requires a fundamental shift from one-way industrial system to circular system model. In circular system, the waste is exchanged in inter-industry either as a resource or as a part of input materials.

Inter-industry cooperation for waste recycling purposes is, however, considered beneficial not only because of the high importance of environmental protection but also waste recycling networks in many cases have further (economic or technical) advantages over internal process chains of industry [1]. Therefore, industrial waste remains a focus of interest in a sustainable industrial development. Waste sector is being managed to contribute to the improvement of industrial redesign and to the connection to industrial recycling networks. Much attention should be devoted in the waste sector such as intensive research to characterize and recover potential value of waste. By acknowledging its potential value, the waste can be valorized as functional materials that may benefit for internal process chains as well as waste recycling networks with inter-industry.

The scope of this thesis is characterization and recovery of valuable matters contained in industrial wastes: shell waste and glass-polishing sludge. These wastes are present in

considerable volume in pearl oyster farming companies and in glass industries, respectively. Optical characterization was utilized to investigate properties of valuable matter-containing wastes that allow them to be designed in a particular purpose according to their native properties towards functional materials. Recovery will mean valuable matter recovery, for example, attempting to extract fluorescent matter from the shell or to separate rare earth elements from glass-polishing sludge.

1.1.1 Pearl oyster farming and shell waste

Pearl oysters are members of the phylum *Mollusca* and belong to the class *Bivalvia*. *Bivalve mollusks* are distinguished by having two shells (two valves) and a soft body. They appear to grow best in clear water that free from large amounts of sediment. They are widely distributed throughout Persian Gulf, Red Sea, Mediterranean Sea and throughout the Indo-Pacific as far as Japan and Australia. Life cycle of pearl oyster in pearl oyster farming is shown in Figure 1.1. Baby oysters, called spat, are born in hatcheries of oyster farm and grown in tanks at the pearl oyster farms. They are matured in baskets in ocean waters after they are 60 days old. After they have grown stronger spending 2–3 years in the water, they are large enough to withstand grafting, a surgically implanting an artificial nucleus (irritant) into the tissue of a pearl oyster. Then, an irritant is inserted into the mature ovary tissue around which lustrous nacre is formed. The oysters are then returned to the water by stringing them on net pocket panel or placing them in oyster baskets suspended from rafts. The pearl oysters should be allowed to rest in very calm waters for about 40 days after grafting before they are inspected because that is when most deaths or nucleus rejections occur. During the post grafting culture, the pearl exterior forms over time and fluctuates with water temperature

and other conditions. It usually takes about 1½–2 years to form a pearl with sufficiently thick nacre 0.8–0.12 in or (2–3 mm) to harvest. The oysters are left suspended for 1–2 years depending on the desired finished diameter of the pearl. The pearls are carefully cut out of the oyster's flesh and separated from the shell. The extracted pearls are processed for sale and wasted shells are traditionally recycled to be jewelry, buttons and other decorative items and ornamentation.

Nowadays, by the application of technology, wasted oyster shells have been investigated to be recycled with various functions such as, calcium resource [2], gas absorbent [3], etc. Also, bivalvia shells have been used extensively as successful bio-monitors recording their life history and information of environmental changes preserved through structural, morphological, and chemical changes within the shell [4, 5].

In Uwajima city, southwestern part of Ehime prefecture, Japan, number of pearl culturing companies are 607 with total production of pearls reached 24,051 kg (24 tons) [6]. It is estimated that producing 1 gram of pearl will produce 30 gram of shell wastes. Research and development is needed to find sustainable way to recycle the wasted shells or to recover valuable matter towards functional materials. In this thesis, the shell was characterized to acknowledge the properties of shell specially origin and distribution of fluorescence matter. The fluorescence matter distribution might be an indication of certain condition of the pearl oyster during growth period for example, sea environment and climate change, metabolism of the pearl oyster and quality level of the pearl in the shell.

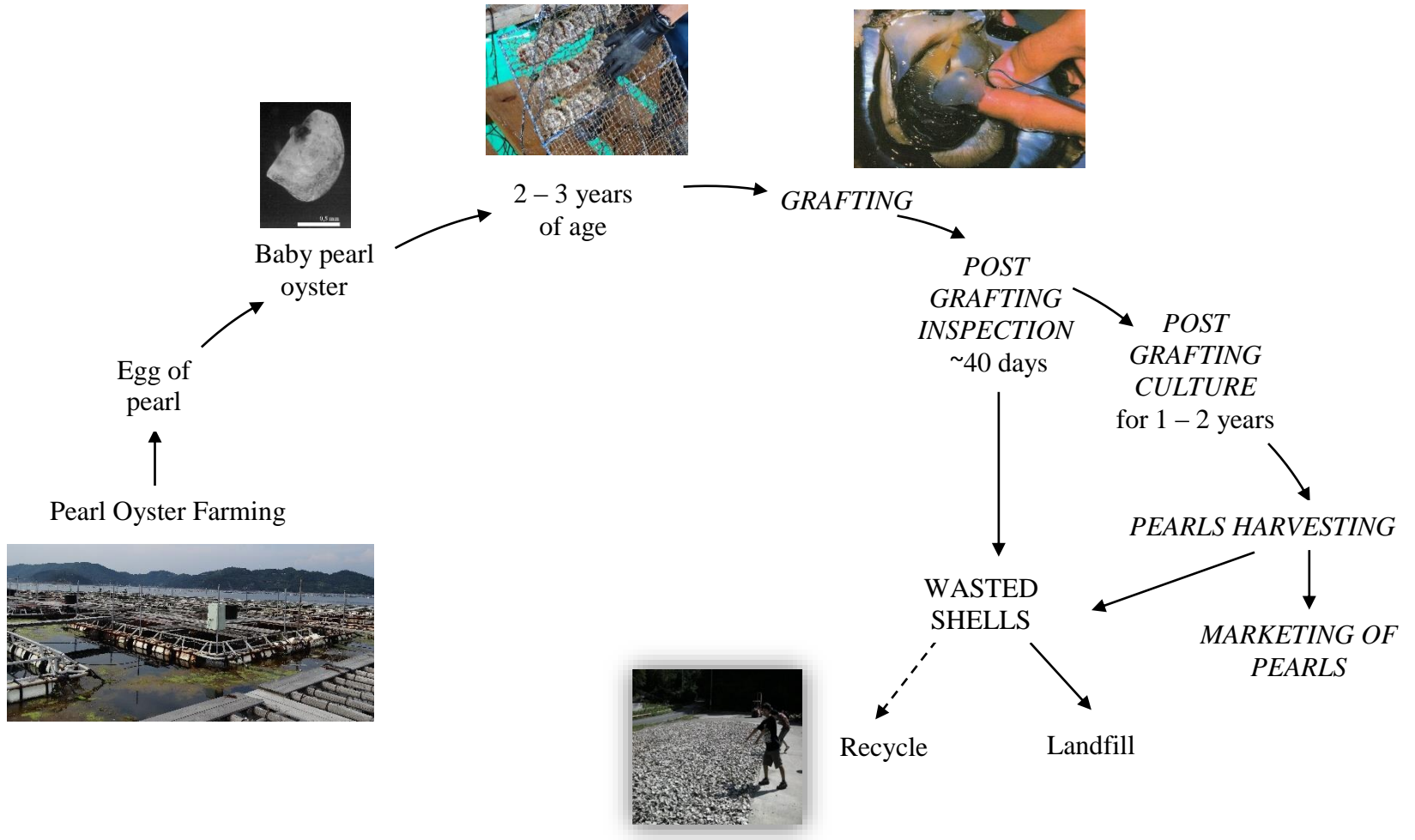


Figure 1.1 Pearl oyster farming process and shell waste

1.1.2 Rare earth-containing glass-polishing sludge and metallurgical slags

Glass has wide range of applications and uses depending on its source of raw materials. Soda lime glasses are for container glasses, tableware and flat glass. The crystal tableware, TV screens and display screen equipment are made of lead glasses. The borosilicate and aluminosilicate glasses are for making glass fibers, wool insulation, ovenware, thermo flasks and for scientific and optical apparatus.

The total world production of optical glass is about 20,000 tons/year [7]. Optical glass used for optical equipment includes a large quantity of rare earth elements for improving its optical characteristic. Lanthanum-containing glass has a high refractive index and a low dispersion, and it is therefore very suitable for the manufacturing of lenses. Special optical glass for use in lenses of cameras, microscopes, binoculars or microscopes can contain more than 40 wt% of La_2O_3 while some optical glasses contain Y_2O_3 and Gd_2O_3 , in addition to La_2O_3 [7]. Rare earth elements are vital components not only for glass technology but also for green technology. However, their natural reserves are only concentrated in few countries and their supplies are strictly delimited. Moreover, they have hardly effective substitutes, low recycling rate, and unsustainable primary mining [8]. Therefore, exploring rare earth elements from secondary resources such as industrial waste is necessary in order to maintain their sustainability.

Production process of optical glass involves series of stages. Each stage has its own input, out-put and there is possibility of waste generation. For example, glass-polishing sludge with glass particles are waste generated from mechanical and chemical polishing stage.

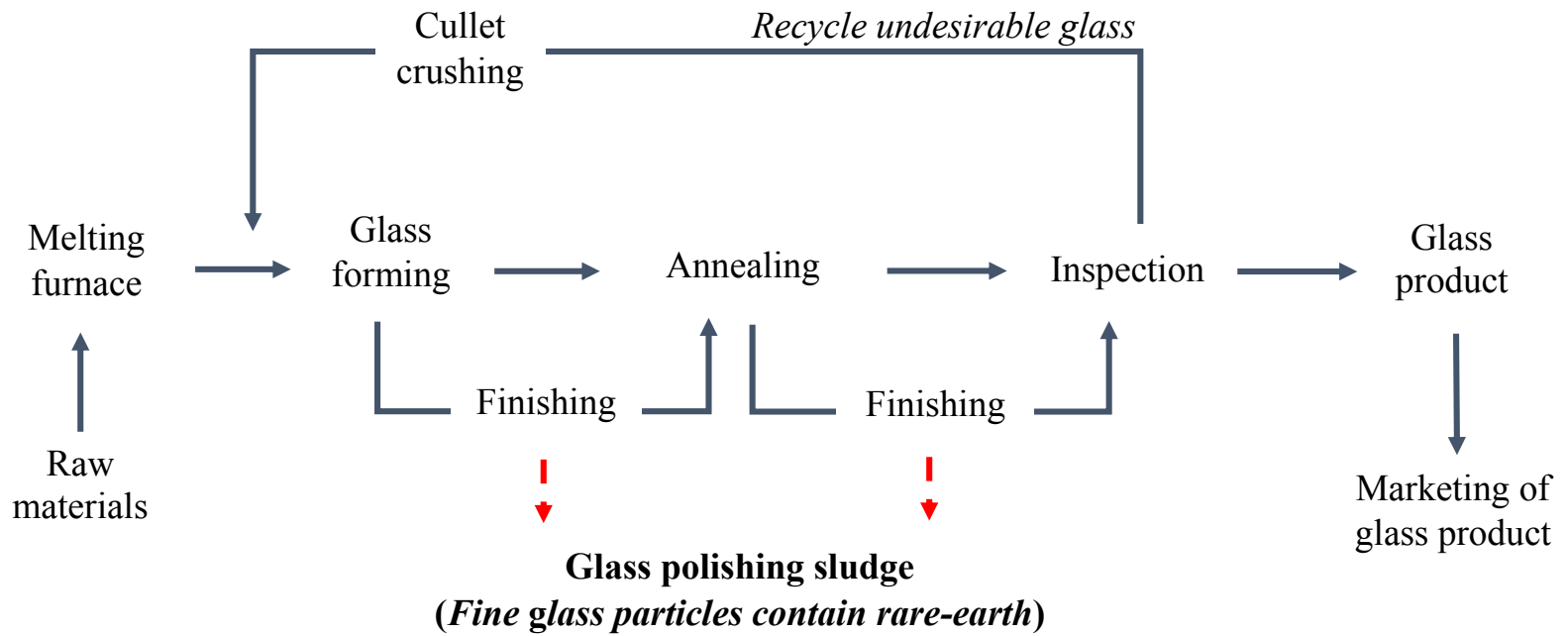


Figure 1.2 Production process of glass showing cullet recycle and generation of glass polishing sludge.

Because of optical glass composition, the glass particles might contain rare earth elements. However, the rare earth elements are always found in low concentration due to incorporating of wastes from other stages of process chains. In this case, glass-polishing sludge brings not only rare earth-containing glass particles but also contaminant such as cerium and alumina particles from hydrolysis of poly(aluminum chloride) as a flocculant of glass-polishing slurry. This issue is also found in metallurgical slag, an industrial waste from metal production process.

Rare earth-containing metallurgical slags are reported in many metal productions. For instance, in iron-making process with magnetite ore containing monazite ores as feeds, 3–9 % of rare earths report to slag [9], and fluoride-type iron ores containing greater than 7.5 % of rare earth elements end up in slag [10]. Likewise, red mud, by-product of alumina production, contains 0.1–1 % of rare earth elements [11, 12]. Even though their concentrations are very low, in fact, these slags are present in considerable volumes. As consequence, the total amounts of trapped rare earth elements in the slags are large enough and might be a promising secondary resource of rare earth elements.

Despite their low concentration in industrial waste, rare earth elements preferentially unite with slag due to their higher chemical affinity into oxygen rather than into metal alloys such as in the case of recycling spent batteries by pyrometallurgical process. In an investigation of slag system $\text{SiO}_2\text{--CaO}$ melted with spent Ni-MH batteries, it was revealed that almost all rare earth oxides from the batteries are selectively precipitated in the solid phase of $\text{SiO}_2\text{--CaO--Re}_2\text{O}_3$ and separated from metal alloys [13]. Similarly, a number of systematic slag composition $\text{SiO}_2\text{--CaO--MgO}$ and CaO--CaF_2 have been investigated and

found that composition of 35CaO–65CaF₂ (wt %) delivered the best separation between Ni-Co alloys and high concentrated rare earth oxides that are accumulated in the slag [14]. Low concentration and a tendency of rare earth elements to accumulate in slag system bring about less economic value to recover the elements by pyrometallurgical process. Meanwhile, hydrometallurgical process needs large consumption of chemicals and releases new chemical residues that are harmful for environment. In order to make efficient recovery, an idea comes up that the rare earth elements in slag system are required to concentrate in such a solid phase that solubility of rare earth into acid increase [7]. A recent study related to this manner dealt with recycling of Nd–Fe–B magnet [15]. The study revealed that, in the slag system Al₂O₃–CaO–MgO–P₂O₅–SiO₂, rare earth elements show strong affinity into a certain phase called britholite phase (silico–phosphates crystallites) then forming solid rare earth-rich phases. It was believed that rare earths enriched in this phase would be easy to recover.

In this thesis, rare earth element-containing glass particles from glass-polishing sludge are characterized to estimate effect of phosphate addition after pyrometallurgical process. On the basis of our previous research revealing composition condition of P₂O₅ to coordinate with rare earth ions in phospo-silicate glass system, we hypothesized in this present investigation that rare earth elements preferentially coordinate with phosphate rather than with silicate in multi-component system of glass particles. Then, by controlling phosphate composition, the rare earth element in the glass can be recovered without acid treatments.

1.2 Purpose and construction of this study

The main objectives of this thesis are characterization of shell waste, *Pinctada vulgaris* from pearl oyster farming and recovery of rare earth elements from glass-polishing sludge.

Several experiments were arranged to achieve the objectives. Fluorescence spectroscopy was utilized to characterize properties of substance or elements contained in the sample, then followed by thermogravimetric / differential thermal analysis (TG/DTA), x-ray diffraction and fourier transform infrared (FTIR) spectroscopy, scanning electron microscopy / energy dispersive spectroscopy (SEM/EDS) and inductively coupled plasma-mass spectroscopy (ICP-MS).

Characterization of pearl oyster shell is aimed to locate the distribution of fluorescence matter and identify the presence of organic substances, composition, and elements composed the shell. Extraction of fluorescent matter was conducted by using acid treatments and chromatographic column. Then, we confirm the fluorescent matter by identifying excitation and emission spectra and compare to spectra of porphyrin. Details of experimental procedures, results and discussion of these experiments are presented in chapter 2.

Recovery of rare earth elements incorporated with glass particles from glass-polishing sludge are conducted by melting the rare earth element-containing glass particle with P_2O_5 addition, and then leached into water. A series of P_2O_5 concentrations were introduced to rare earth-containing glass particles. The effect of P_2O_5 addition upon recovery of rare earth elements was investigated by utilizing fluorescent spectroscopy and inductively coupled

plasma-mass spectroscopy (ICP-MS). Details of experimental procedures, results and discussion of these experiments are presented in chapter 3. Chapter 4 is general conclusion of this thesis.

References

- [1]. Posch A (2010) Industrial Recycling Networks as Starting Points for Broader Sustainability-Oriented Cooperation. *Journal of Industrial Ecology*. 14(2):242-257.
- [2]. Onoda H, Nakanishi H (2012) Preparation of calcium phosphate with oyster shells. *Natural Resources*. 3(2):71.
- [3]. Jung J, Yoo K, Kim H, Lee H, Shon B (2007) Reuse of Waste Oyster Shells as a SO₂/NO_x Removal Absorbent. *Journal of Industrial and Engineering Chemistry-Seoul*. 13(4):512.
- [4]. Nuñez JD, Laitano MV, & Cledón M (2012) An intertidal limpet species as a bioindicator: Pollution effects reflected by shell characteristics. *Ecological Indicators*. 14(1):178-183.
- [5]. MacFarlane GR, Markich SJ, Linz K, Gifford S, Dunstan RH, O'Connor W, Russell RA (2006) The akoya pearl oyster shell as an archival monitor of lead exposure. *Environmental Pollution*. 143(1):166-173.
- [6]. http://web-japan.org/atlas/nature/nature_fr.html, 1995.
- [7]. Binnemans K, Jones PT, Blanpain B, Van Gerven T, Pontikes Y (2015) Towards zero-waste valorisation of rare-earth-containing industrial process residues: a critical review. *J Clean Prod* 99:7–38.
- [8]. Massari S, Ruberti M (2013) Rare earth elements as critical raw materials: Focus on international markets and future strategies. *Resour Policy* 38:36–43.

- [9]. Kim CJ, Yoon HS, Chung KW, Lee JY, Kim SD, Shin SM, Lee SJ, Joe AR, Lee SI Yoo SJ (2014) Leaching kinetics of lanthanum in sulfuric acid from rare earth element (REE) slag. *Hydrometallurgy* 146:133–137.
- [10]. Zheng X, Lin H (1994) Mineralogy and flotation of rare-earth-bearing barium fluorophlogopite. *Miner Eng.*
- [11]. Ochsenkühn-Petropulu M, Lyberopulu T, Ochsenkühn KM, Parissakis G (1996) Recovery of lanthanides and yttrium from red mud by selective leaching. *Anal Chem Acta* 319:249–254.
- [12]. Tsakanika LV, Ochsenkühn-Petropoulou MT, Mendrinou LN (2004) Investigation of the separation of scandium and rare earth elements from red mud by use of reversed-phase HPLC. *Anal Bioanal Chem* 379:796–802.
- [13]. Tang K, Ciftja A, Van Der Eijk C, Wilson S, Tranell G (2013) Recycling of the rare earth oxides from spent rechargeable batteries using waste metallurgical slags. *J Min Metall Sect B Metall* 49:233–236.
- [14]. Müller T, Friedrich B (2004) Development of a CaO-CaF₂ -slag system for high rare earth contents. *Molten slags fluxes and salts* 449–454.
- [15]. Elwert T, Goldmann D, Schirmer T, Strauß K (2014) Affinity of rare earth elements to silico-phosphate phases in the system Al₂O₃-CaO-MgO-P₂O₅-SiO₂. *Chemie Ing Tech* 86:840–847.

Chapter 2

Optical characterization of fluorescent matter in prismatic layers of *Pinctada vulgaris* shell

2.1 Introduction

Optical properties of molluscan shells such as luminescence (phosphorescence and fluorescence) and iridescent color have attracted interest of scientists for long time. The structure of molluscan shell plays important role of absorbing, transmitting and reflecting light. Some mollusks can produce fluorescence, and their shells selectively transmit and absorb some of the light [1, 2]. Other mollusks such as *Gastropoda* and *Bivalvia* are unable to produce fluorescence but their structural shells express iridescent colors. The shell generally constitutes of nacre layers in inner side and prismatic layers in outer side (Figure 2.1). Iridescent color mostly appears on the nacreous layers. Several investigations have been done to reveal this rainbow color on the nacre layers. For instance, in the nacre of *Gastropoda*, *Haliothis glabra*, the regular stack structure brings about a series of color such as violet, green and red due to interference of light [3]. *Helcion pruinosus* has typical

structure only at particular spots with bright green color on the nacre. The green color comes from the light reflected by a layered quarter-wave stack embedded approximately 50 μm below outer surface and tilted by approximately 24° [4]. Likewise, *Pinctada margaritifera* has strong iridescent color shining on the nacre caused by diffraction of light on the high groove, smooth and fine structure [5].

Meanwhile, prismatic layer does not demonstrate iridescent color. Unlike nacreous layers with their structure relatively regular, prismatic layers compose of irregular and polygonal columns of calcite crystal, and are separated by inter-prismatic organic membranes [6, 7]. As the outer part of shell, prismatic layers contact directly to severe condition, such as seawater and other oceanic living organisms. In consequence, their surface become rough, coarse, and cannot create optical interference or diffraction effects. In fact, many organic substances occupy prismatic layers, for example, sulphur amino acids and conchiolin [8-10]. These proteinous substances might include melanins, pyroles, and porphyrins [11] as fluorescent compounds. These compounds are abundantly found in prismatic layers of *Pinctada vulgaris* well known as Persian lingah oyster [12]. Porphyrins are recognized as fluorophores with high intense fluorescence because have extensive system of electron transitions called Soret band (380–500 nm) and Q-bands (500–750 nm) [13]. Thus, optical properties of prismatic layers of *Pinctada vulgaris* would be fluorescence due to the presence of porphyrin. However, as far as we know, there are no studies well explaining about the distribution of fluorescent matter in the prismatic layers of *Pinctada vulgaris*. Most of the studies are classifying the proteineous substances by extracting prismatic layers.

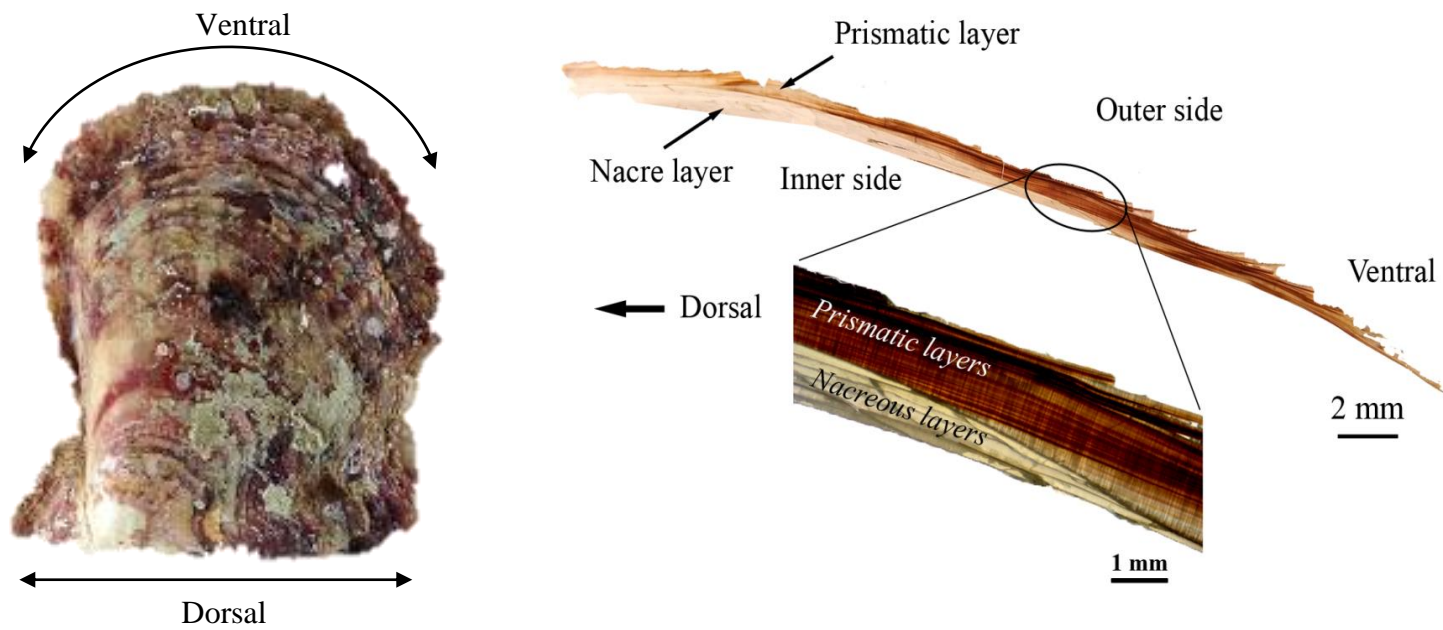


Figure 2.1 A shell of *Pinctada vulgaris* and its cross section showing prismatic layers and nacre layers.

The purpose of this work is to study the distribution of fluorescent matter in the prismatic layers of *Pinctada vulgaris* by fluorescence microspectroscopy. We also need to confirm the fluorescent matter by identifying excitation and emission spectra and compare them to spectra of porphyrins. Characterization of prismatic layers was also conducted to identify the presence of organic substances, composition, and phase of calcium carbonate as the main element of prismatic layers. Finally, we extract fluorescent matter using acid base extraction and chromatographic column.

2.2 Experimental Methods

Materials used in this study were shells of *Pinctada vulgaris* cultivated in Uwajima, Ehime prefecture, Japan. The shells were cleaned from other oceanic living organisms, immersed in purified water at 40°C in an ultrasonic cleaner for 5 hours to eliminate seawater contaminants, and dried at 60°C in a drying chamber for about 30 minutes.

The prismatic layers were irradiated using a commercial UV LED enabling us to distinguish red fluorescent layers. The red fluorescent layers were picked up and separated from nacreous layer then ground to be powder with a diameter of ~100 µm. The powdered samples were examined using XRD, TG-DTA, and spectrophotometer.

Thin section samples were made by cutting the shell perpendicular to its surface from the dorsal to the ventral side and then embedded into resin. The samples were polished with alumina powder and continued with 1 µm diamond slurry until reached ~0.1 mm thickness. Afterward, the thin samples were ultrasonically cleaned in purified water at 40°C for 1 hour to eliminate the remaining diamond slurry. These thin sections were used for microstructure observation, elemental mapping, and fluorescence spectroscopy. The thin section prepared

for microstructure observation was etched in 5 vol% hydrochloric acid for 5 seconds to reveal growth lines and inter-prismatic membranes.

The SEM-EDS experiments were carried out using JEOL JSM-6510 LV with an Oxford X-max 50 detector. The working voltage is at 15–20 kV and the specimen current is between 0.8–2 nA for 6 hours.

Powdered samples were characterized by X-ray diffraction (D38742, PANalytical) using Cu K α irradiation operated at 45 kV and 40 mA. The scanning rate was 0.2°/s in the 2 θ range of 10–90°. Phase identification was made by searching the ICSD powder diffraction file database.

TG-DTA (TG-DTA8120, Rigaku) allows us to observe the thermal decomposition of calcium carbonate as well as organic matters contained in the prismatic layers. It was operated in the temperature range of 25–850°C for prismatic powder with 20 mg at a heating rate of 10°C/min. Heat flow and weight loss were recorded during heating process. The results were compared to the decomposition of *calcium carbonate* reagent (99.5%).

Excitation and emission spectra of prismatic layer were measured by a spectrophotometer (F-7000, Hitachi) with a wavelength resolution of 1 nm. It was operated at scanning rate 240 nm/min with photomultiplier tube voltage of 400 V. Then, the excitation spectrum of powdered sample was referred to determine excitation wavelength for fluorescence microspectroscopy.

A fluorescence microscope (IX70, Olympus) equipped with a mercury lamp (404.7 nm) and a CCD detector (Spectra-Pro 300, ACTON research) was used to determine emission spectra from specific detection spots on the shell and the thin cross section of shell

samples. The mercury lamp (404.7 nm) was chosen because its emission line lies near to the wavelength of maximum absorption of prismatic layers. By setting up the arrangement of objective lens magnification and slit, it enabled us to select emission from 1–50 μm detection spots.

To extract fluorescent matter, a shell should be cleaned from any oceanic living organism stuck on its surface. Shell layers (prismatic layers) were selected under UV light using commercial UV LED, coarsely broken and powdered. 2 gr powdered shell was added in 4 mL HCl in small beaker and they are stirred for about 10 minute and separated solution from precipitate in centrifuge machine. A chromatographic column was used to extract fluorescent matter in acid solution, and then methanol was used to exude fluorescent matter from chromatographic column. These processes were conducted at room temperature.

2.3 Results and Discussion

2.3.1 Microstructure of prismatic layers

Figure 2.2 shows the cross section of prismatic layers polished and etched in hydrochloric acid. The image reveals growth lines (GL) transecting inter-prismatic organic membranes (OM). The inter-prismatic membrane is an envelope composed of organic substances [14] and the growth lines are alternations of rich mineral and rich organic zones [15].

2.3.2 Calcitic prismatic layers

Figure 2.3(a) shows the X-ray diffraction pattern of powdered sample from prismatic layer. Each peak well agrees with the peak of a PDF card (01-085-1108) as shown in Figure

2.3(b). Therefore, it can be determined that phase of calcium carbonate in prismatic layer is calcite. We use the name of calcitic prismatic (CP) layer hereinafter.

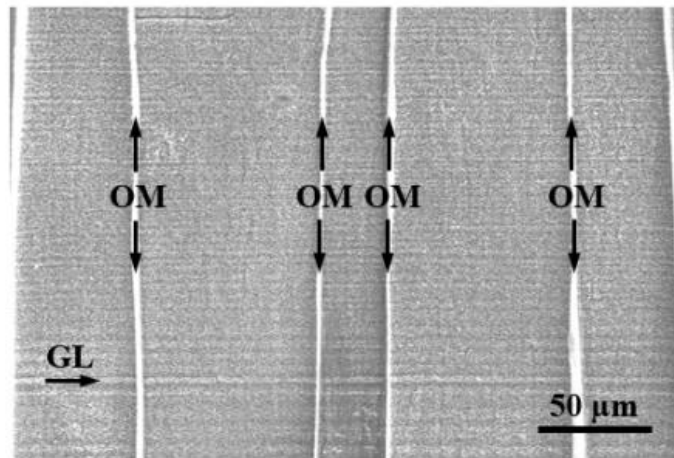


Figure 2.2 Microstructure of calcitic prism (CP) layer. **GL** is a growth line among parallel growth lines. **OM** are inter-prismatic organic membranes.

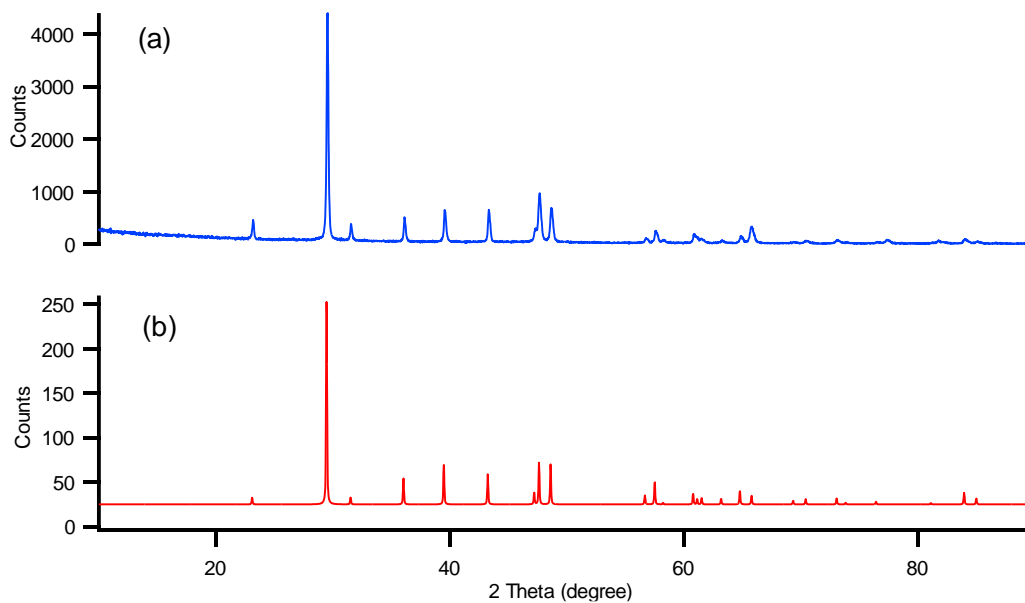


Figure 2.3 X-ray diffraction pattern. (a) CP powdered sample. (b) Calcium carbonate from ICSD powder diffraction file database. Peaks indicate calcite phase.

2.3.3 Thermal decomposition of prismatic layers

Figure 2.4(a) shows DTA curves of heat flow and weight loss of both (CP) layer and calcium carbonate reagent with 99.5% purity. Five weight losses and three exothermic events were detected in CP powdered sample due to thermal decomposition positioning in temperature ranges 25–190°C, 190–383°C, 383–512°C, 512–670°C, and 670–850°C (Figure 2.4(b)). The first weight loss (25–190°C) was attributed to loss of absorbed water. The second to the fourth weight losses corresponding to exothermic reactions of I, II, and III (Figure 2.5(a)) started from 190°C and ended at 670°C, were attributed to burn out of organic substances. Loss of weight in temperature range of 670–800°C was the decomposition of CaCO_3 into CaO and CO_2 . This result supports other investigations about the thermal decomposition of organic substances in prismatic layer of *molluscan* shells [16]. In comparison to calcium carbonate reagent without organic content, thermal decomposition shown in Figure 2.5(b) did not show any exothermic reactions after loss of water content at 25–190°C and before the decomposition of CaCO_3 at 700–800°C. Through this experiment, total organic substances in CP of *Pinctada vulgaris* can be estimated about 7.1 %. This amount is close to the highest organic content ever reported in granular prism of *Entodesma navicula*, ~ 7.4 % [17].

2.3.4 Excitation and emission spectra of prismatic layers

Figure 2.6 shows the excitation and emission spectra of as-grinded and heat-treated CP powdered samples. There is a strong absorption band at 350–460 nm with a peak wavelength of 402 nm. There are also three weak bands with peak wavelengths at 506, 542, and 564 nm. The emission spectrum excited at 402 nm shows three peaks of 621, 652, and

681 nm. The CP powdered sample heat treated up to 383°C after the first exothermic reaction (I) as shown in Figure 2.5(a) showed no emission spectra.

The red fluorescent matter naturally occurred in many molluscan shells is a fluorophore called porphyrin [18]. It is well understood that absorption bands of porphyrin possess two distinct bands [19]. The first band is due to an excitation of electron from the ground state to the second excited state ($S_0 \rightarrow S_2$) called Soret band at 380–500 nm, and the second bands are excitation from the ground state to the first excited state ($S_0 \rightarrow S_1$) called Q-bands consisting of several weak bands between 500–750 nm [19]. The Soret and Q-bands might be shifted depending on insertion of metal ion into the macrocycle molecules, and the fluorescence emission intensity might be changed depending on peripheral substituents on the porphyrin ring [20]. For example, insertion of Co, Ni, and Cu ion on the central part of porphyrin result in blue shift of the Soret bands, and insertion of Mn(II) and Zn(II) promote red shift in the Soret band and decrease the number of Q bands [13].

Compared to the excitation wavelength of CP powdered sample, higher energy state occurred in the strong absorbance in the range of 350–460 nm with a peak wavelength of 402 nm, slightly shifted to the blue region, and lower energy state consists of three weak bands ranging between 500–600 nm. The excitation and emission spectra of our sample closely correspond to the spectra of uroporphyrin that has a 405 nm peak of Soret band and four Q-bands in the range of 500–580 nm, and three peaks of emission spectra at 610–620, 640–650, and 670–680 nm [21]. The presence of porphyrin in *Pinctada fucata* shell especially in the prismatic layers has been also reported and specifically identified as uroporphyrin I [9].

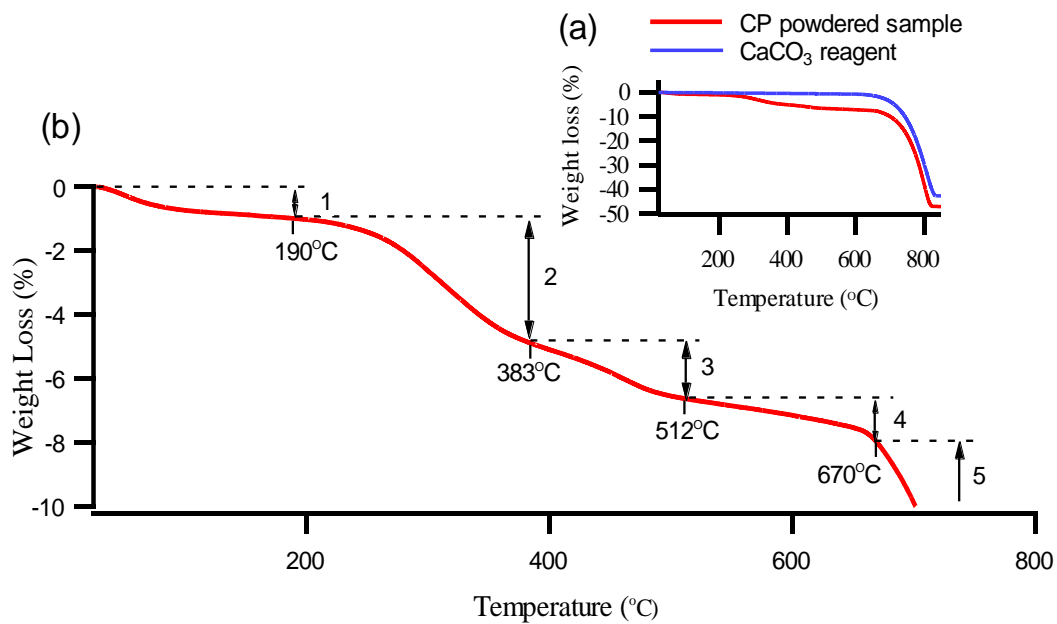


Figure 2.4 Thermal decomposition of prismatic layer and calcium carbonate reagent. (a) Weight loss of CP powdered sample and CaCO₃ reagent (inset). (b) Five weight losses of CP powdered sample (magnified).

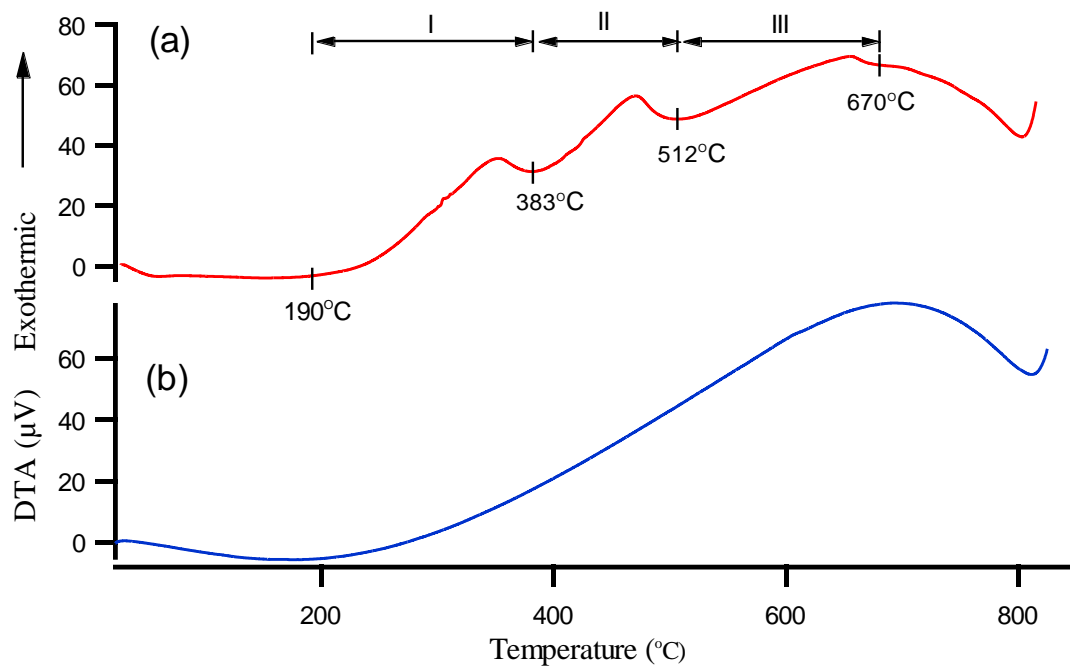


Figure 2.5 Thermal decomposition of prismatic layer and CaCO_3 reagent. (a) Exothermic reaction of CP powdered sample. (b) Exothermic reaction of CaCO_3 reagent.

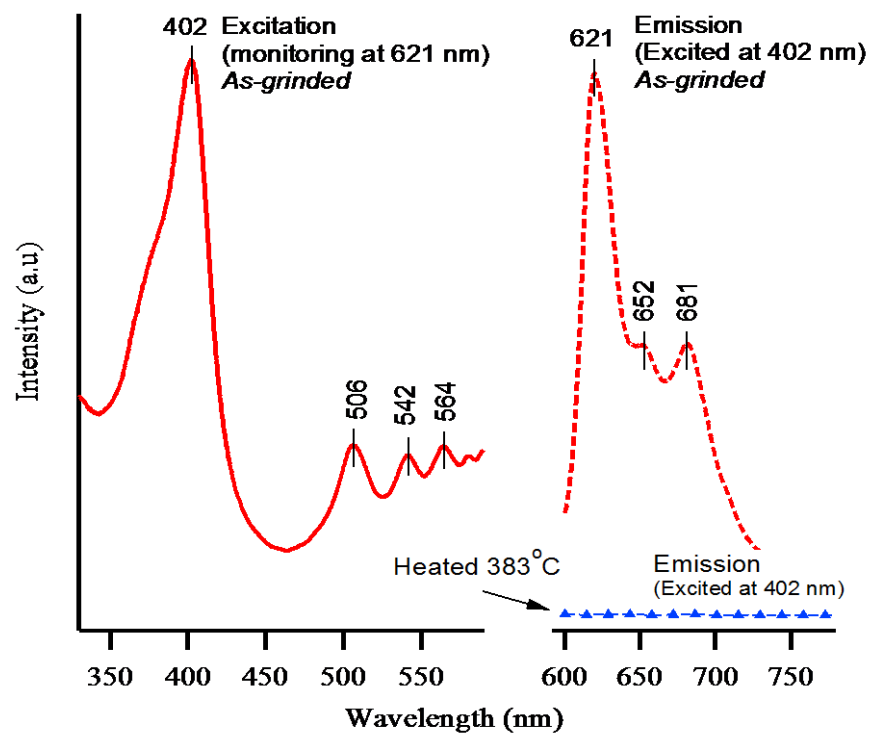


Figure 2.6 Excitation and emission spectra of as-grinded and heated CP powdered samples.

2.3.5 Distribution of fluorescent matter

Figure 2.7 shows the outer surface of shell is fully shielded by CP layer. The distribution of fluorescent matter is demonstrated on the outer and inner surfaces of the shell, and inside CP layers. Under daylight irradiation shown in Figures 2.7(a) and 2.7(b), most of the outer CP layers appeared brownish and some areas appeared pale white. However, when the outer CP layers were irradiated using a commercial UV LED, most of the brownish layers turned to red with fluorescence on almost over the surface whereas some of the pale white area remained pale white as shown in Figure 2.7(c). Figure 2.8 shows the appearance of the inner side of the shell both inner CP layers and nacre. The inner CP only occupies the edge and ventral side of shell while nacre covers large area on the center. When the inner CP layers and nacre were irradiated using a commercial UV LED, some area in the inner CP layers show red fluorescence (Figure 2.8(a)) and few do not show (Figure 2.8(b)), while nacre turns to pale blue (Figure 2.8(a)). In order to confirm whether this fluorescent matter contains porphyrin as observed in the CP powdered sample, the emission spectrum of the inner CP layers was compared to the emission spectrum observed from CP powder sample at an excitation wavelength of 405 nm. We used the excitation wavelength of 404.7 nm on a mercury lamp as an excitation light in the fluorescence microspectroscope because this wavelength is within the range of the Soret band (350–425 nm).

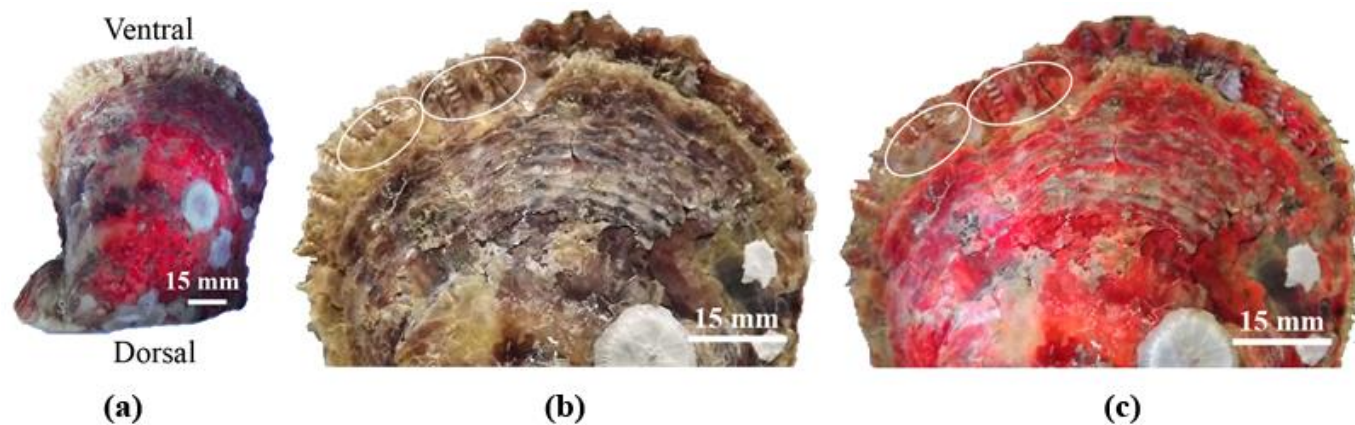


Figure 2.7 Shell of *Pinctada vulgaris* after being cleaned from oceanic living organism. (a) Outer side of shell shielded by CP layers irradiated by daylight (left side) and commercial UV LED (right side). (b) and (c) Close up of ventral side of shell under daylight and commercial UV LED irradiations, respectively. The circles show areas where the brownish CP layers turn to red whereas pale white unchanged.

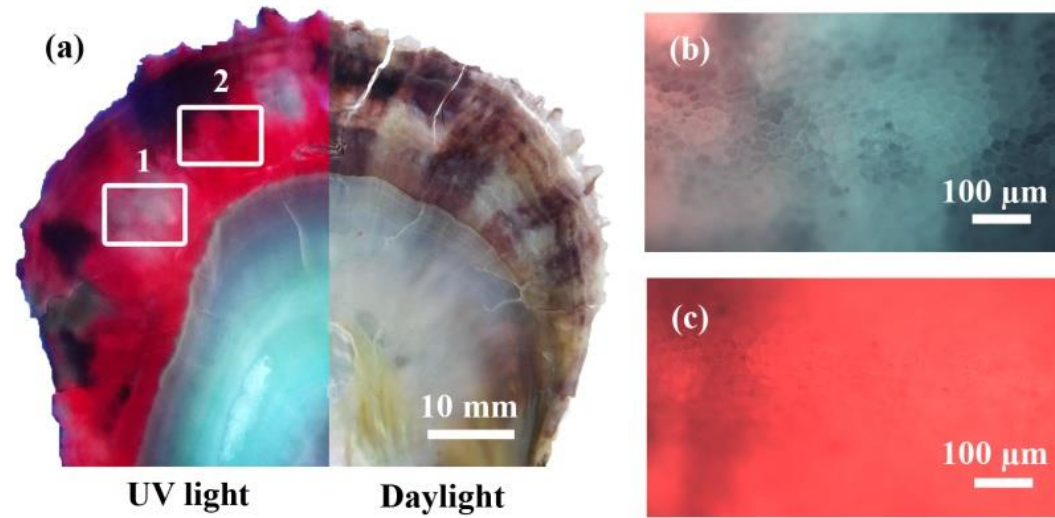


Figure 2.8 An inner side of shell (*Pinctada vulgaris*). (a) Inner shell irradiated by commercial UV LED (left side) and daylight (right side). (b) and (c) Area 1 and 2 respectively, that turn to pale blue and red, under commercial UV LED irradiations. Irradiated area size is ~1 mm.

To minimize deviation of the excitation wavelength measured by spectrophotometer, CP powdered sample was excited at 405 nm close to the excitation wavelength 404.7 nm used in a fluorescence microspectroscope. Then, the emission spectrum of CP powdered sample (405 nm excitation) is referred to find the consistency of emission wavelength of both samples; inner CP layers and thin section CP layers.

Figure 2.9 shows the emission spectrum selected from the red fluorescence (area 2) on the inner CP layers (Figure 2.8(c)). The three emission peaks have consistent wavelengths with a powdered sample. This indicates that red fluorescence emission on the area 2 is also due to porphyrin.

Figure 2.10 shows the distribution of fluorescent matter inside CP demonstrated on a thin cross section sample taken from ventral side of shell (Figure 2.10(a)). Under 404.7 nm light irradiation, the CP layers emit red fluorescence and only some CP layers show pale blue. The fluorescent matter dominates every CP layer transecting several organic membranes (Figures 2.2, 2.10(b) and 2.10(c)). It lies over, under and between each other forming lamellar pattern consisting of red and black parallel zones (Figure 2.10(d)). It is necessary to monitor fluorescence emission spectra in the red and black lamella since compositional alternation may derive to the intensity modulation of red fluorescence. We select area 3 (Figure 2.10(d)) because the thickness between red and black lamellae is large enough to magnify and record the emission by a fluorescence microspectroscope.

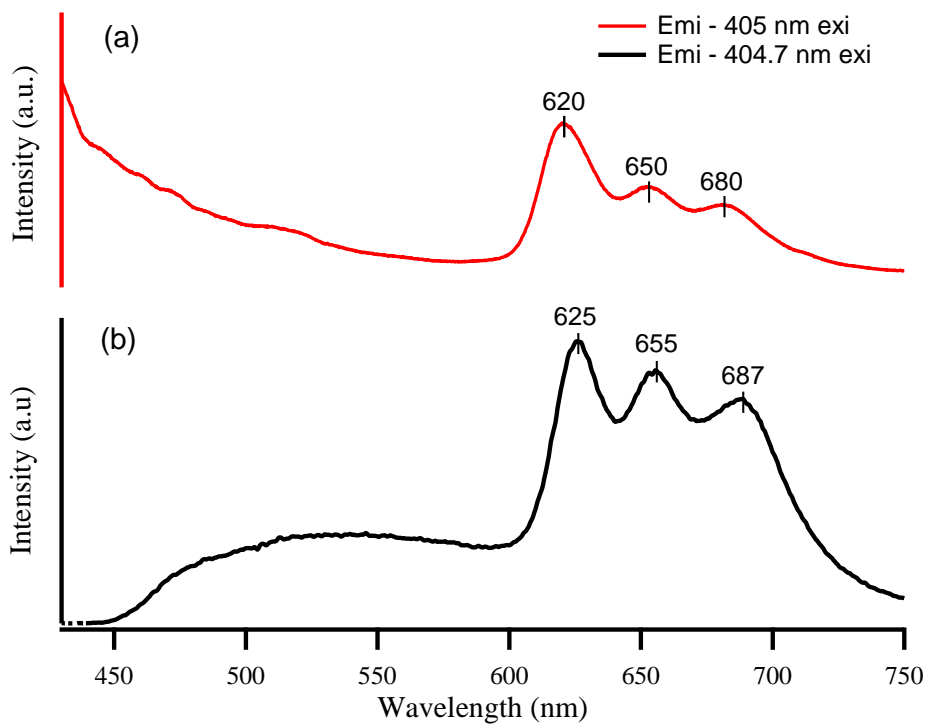


Figure 2.9 Emission spectra of CP powdered sample and inner CP layer. (a) Emission spectrum of CP powdered sample excited at 405 nm. (b) Emission spectrum of inner CP layer on the area 2 in the Figure 2.8(c) excited at 404.7 nm. Detection spot size is $\sim 50 \mu\text{m}$.

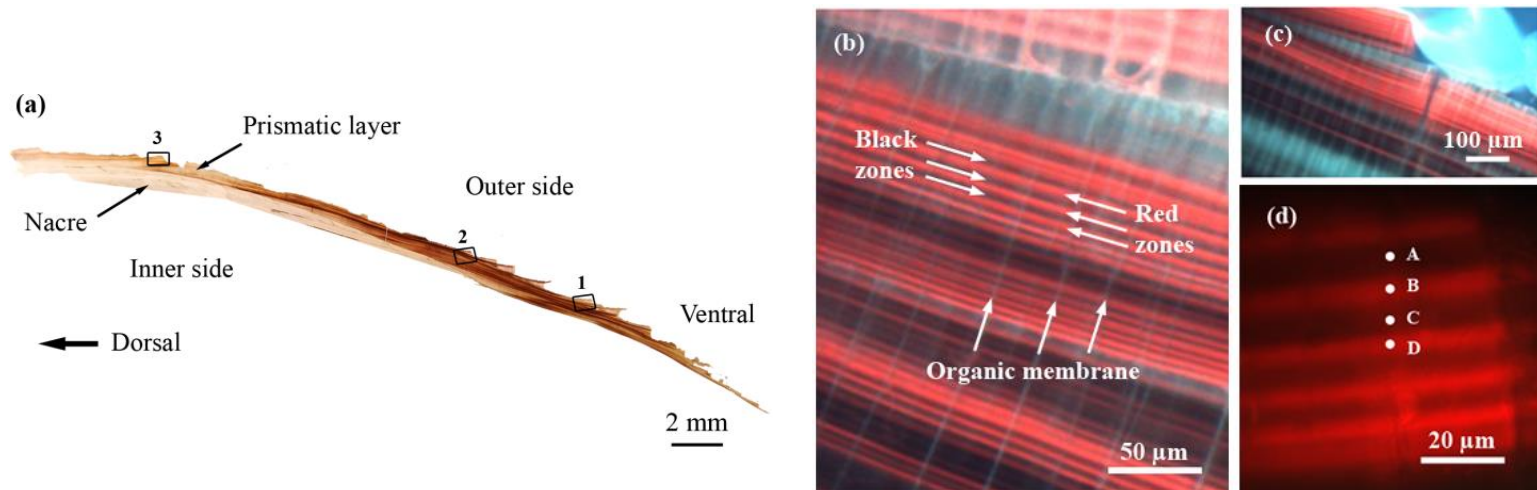


Figure 2.10 Cross section of shell and CP layers under 404.7 nm irradiation showing lamellar pattern formed by red fluorescence and black lamellae. (a) Nacre as inner side of shell fully covered by the calcitic prism in the outer side. (b) Area 1 on CP layers showing red parallel lines and organic membranes. (c) Area 2 on CP layers. (d) Area 3 on CP layers selected for measuring emission from red and black lamellae. Irradiated area size is ~200 μm–1 mm.

As shown in Figure 2.11, emission spectra on the red fluorescent lamella on B and D spots appeared into three peak wavelengths namely 628 nm, preceded by 652–653 nm and 690 nm, slightly shifted to red region compared to CP powdered sample (Figures 2.11(a) and 2.11(b)). The emission intensity of B and D spots are nearly equal. On the other hand, the black lamellae on A and C spots in area 3 (Figure 2.10(d)) have emission wavelengths with similar peaks of 627, 650–652, and 687 nm but the emission intensities are relatively lower than those of red lamellae (B and D spots).

2.3.6 Lamellar pattern of fluorescent matter

Lamellar arrangement in the prismatic shell was formed during the regular growth rhythms associated with bio-mineralization of shells. It was initiated by living mollusc (the mantle) extended from the shell and secreted immiscible liquids (viscous organic and extrapallial fluid) forming polygonal cavities through interfacial tension on viscous organic fluid, while extrapallial fluid became spore of calcite crystals filling the polygonal cavities, afterwards bio-mineralization started [16]. The mantle proceeded extending and retracting movement to create new layers below the previous one [22, 23]. During bio-mineralization, organic substances were deposited alternately with calcite crystals, therefore, prismatic layers show lamellar arrangement [6] as shown in Figure 2.2 (GL). In prismatic layers of *Pinna nobilis* shell, some elements such as magnesium and sulphur have been detected following such lamellar pattern with the alternating zonation of magnesium rich and sulphur rich [24].

As shown in Figures 2.10(b)–2.10(d), under 404.7 nm irradiation, CP layer displays red fluorescence pattern. The pattern appears as a number of red parallel lines transecting organic membranes. In higher magnification, it appears as lamella composed of red and black

parallel zones stacking each other. The lamellar pattern of red fluorescence is acceptable because of following lamellar growth arrangement of calcitic prism of pinctada shells. The calcitic prismatic layer, in fact, comprises lamellar arrangement of calcium carbonate and organic substances. These lamellae are arranged by interchanging the ratio of calcium carbonate and organic substances. For instance, growth lines in lamellar prismatic layers are narrow zonations, containing organic substances with much higher concentration than in adjacent zones [22]. As shown in Figure 2.11(b), the red parallel zones, B and D points, emit light in high intensity of red fluorescence whereas the black zones, A and C points, emit light nearly half lower than B and D points' intensities. Therefore, further observation on the black zone with low emission intensity was conducted. We marked the most black and wider region on the shell sample as shown in Figures 2.12(a) and 2.12(b). As shown in Figure 2.13(b), the emission spectrum of black region (F point) shows similar wavelength profile to the emission spectrum of CP powdered sample (Figure 2.13(a)). In other words, porphyrin compound is also contained in the black region. However, as shown in Figure 2.12, the emission intensity of F point is 10 times lower than that at E and G points, and the F point is recorded by CCD camera as a black color zone.

Elemental mapping analysis, shown in Figures 2.12(c) and 2.12(d), indicate the existence of sulphur-rich zone occupied the same region as the black region denoted F point in Figure 2.12(b). Point elements analysis was also conducted to quantize the weight percent of sulphur element. The result also showed concentrated sulphur element on marked area. On this area, sulphur was approximately detected at 0.2 weight %.

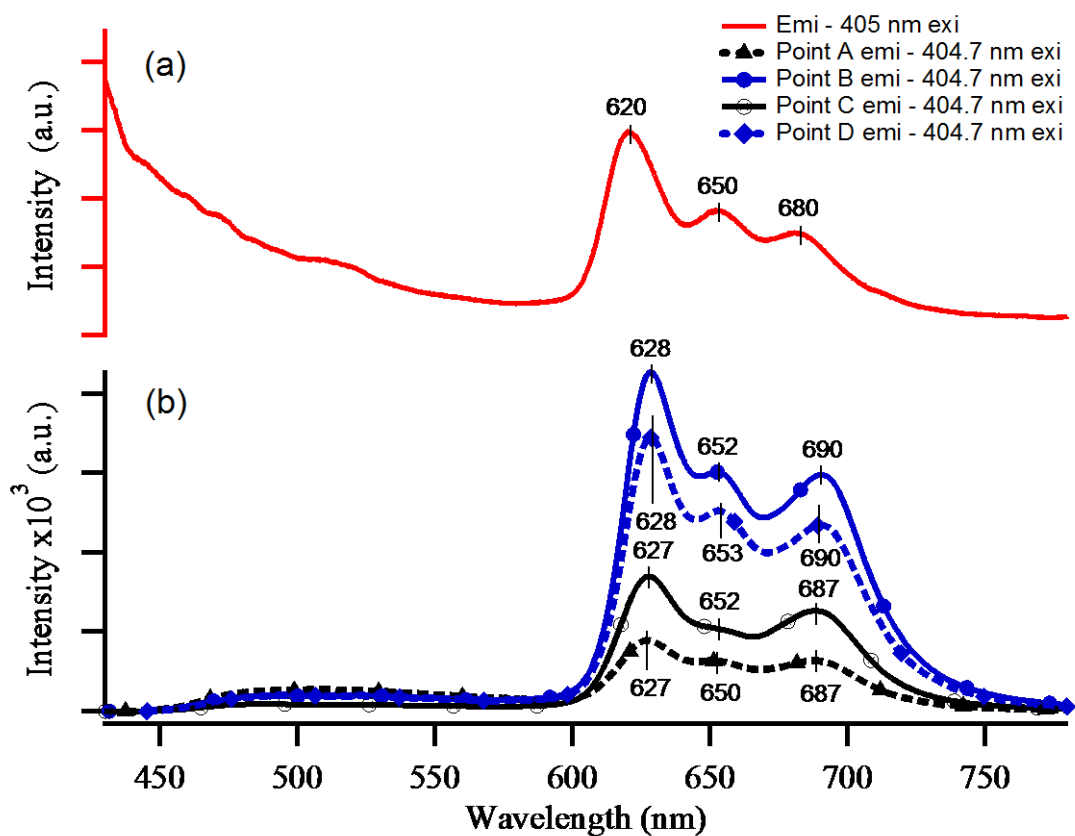


Figure 2.11 Emission spectra of CP powdered and CP thin cross section sample. (a) Emission spectrum of CP powdered sample excited at 405 nm. (b) Emission spectra measured on A, B, C and D spots in lamellar pattern of area 3 as shown in Figure 2.10(d). Red lamellae are the lamellae occupied by organic substance related porphyrin structure. Detection spot size is $\sim 1 \mu\text{m}$.

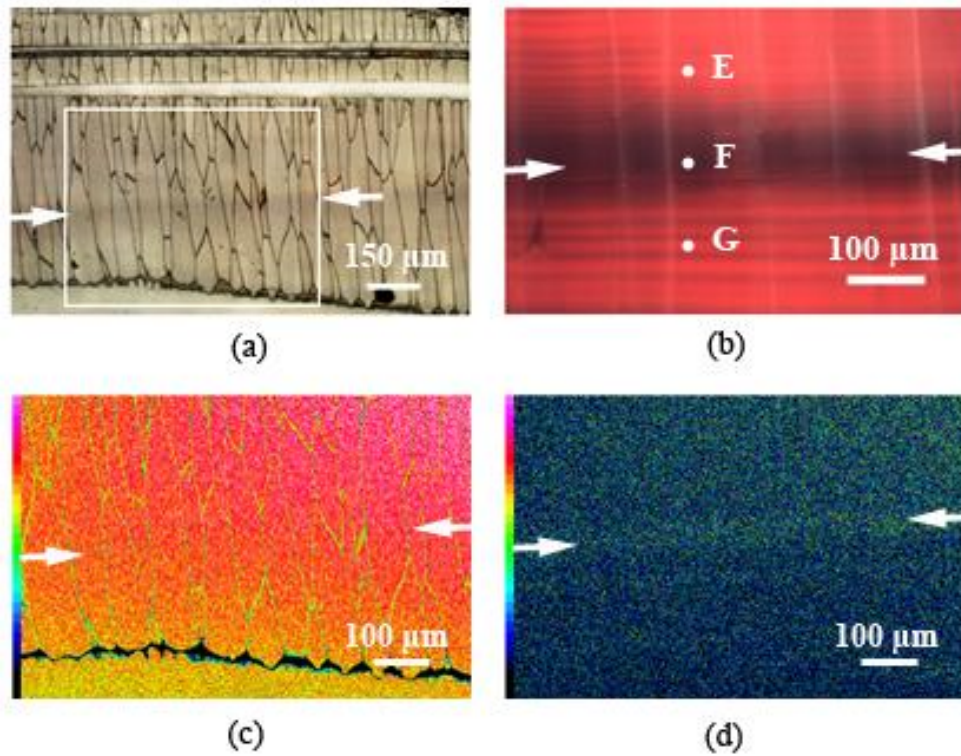


Figure 2.12 Marked area and Elemental mapping on CP layers. (a) Marked area in CP shell sample. The arrows show location of black zone. (b) The marked area, under 404.7 nm irradiation, showing the most black and wider zone between red fluorescent zones. (c) Calcium map of marked area, showing calcium is not concentrated on the black zone. (d) Sulphur map of marked area, showing rich sulphur is concentrated on the black zone than on the adjacent area.

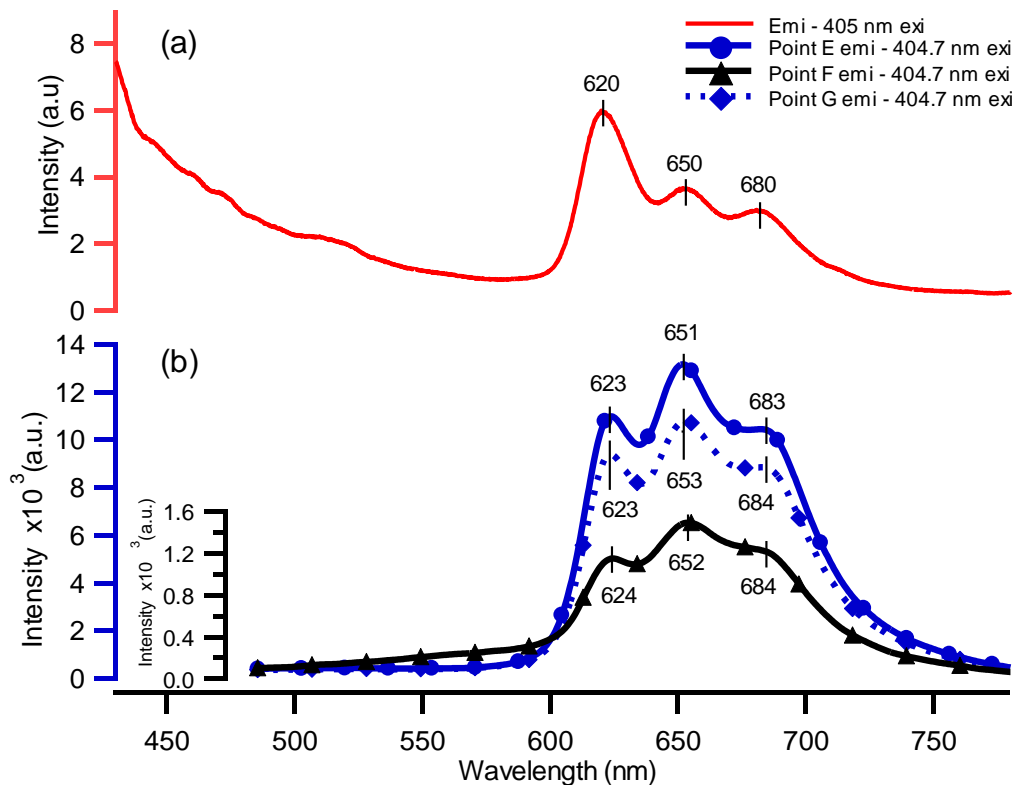


Figure 2.13 Emission spectra of CP powdered and CP thin cross section sample. (a) Emission spectrum of CP powdered sample excited at 405 nm. (b) Emission spectra measured on E, F, and G points in lamellar pattern as shown in Figure 2.12(b). Detection spot size is $\sim 10 \mu\text{m}$.

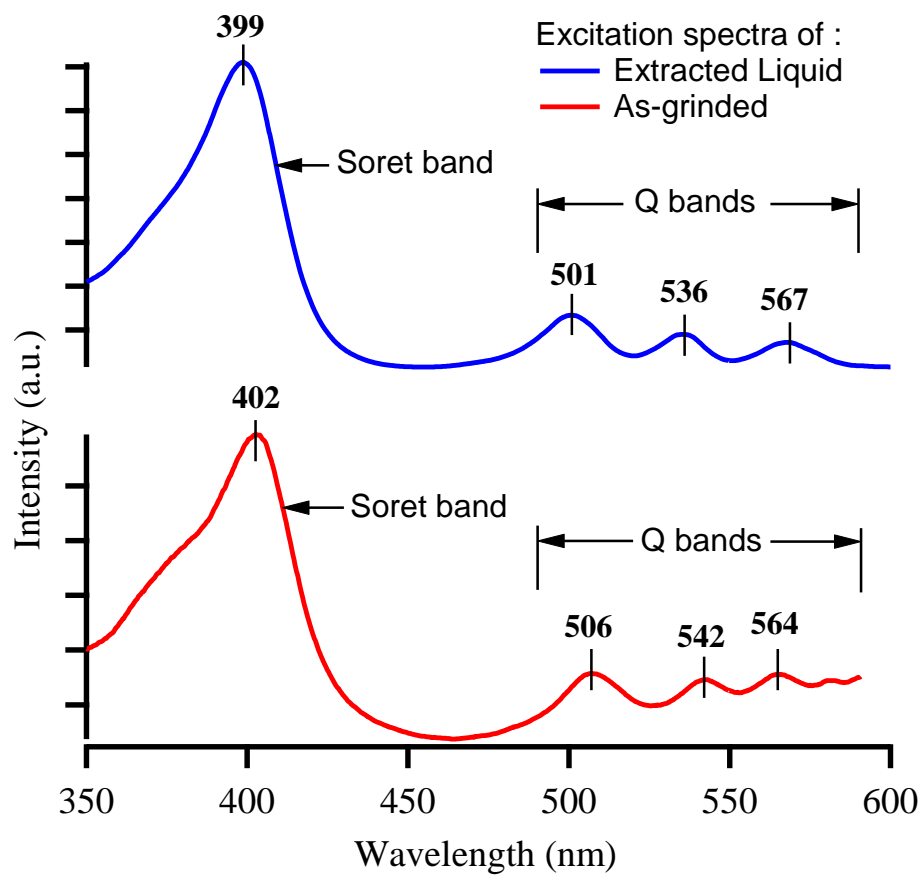


Figure 2.14 Excitation spectra of extracted liquid and CP powdered.

This amount is comparable to the amount of sulphur elements ever been reported at 0.31 weight % in *Pinctada* shell [24]. Our elemental mapping analysis is in agreement with previous results as follows. The presence of sulphur-rich zones has been also confirmed in the prismatic layer of *Pinctada margaritifera* [8] and *Pinna nobilis* [24]. Other possibility is that porphyrin concentration affects the modulation intensity. However, we cannot firmly conclude. We can only suggest that the red-black lamellar fluorescence pattern corresponds to porphyrin-rich and sulphur-rich zones.

Extraction process using HCl and chromatographic column were successful to absorb fluorescent matter liquid. Absorption band similarity between the extracted liquid and the CP powdered sample (as-grinded) shown in Figure 2.14 indicates that porphyrin-containing organic substances didnot change due to acid treatment during the process of extraction.

2.4 Conclusion

Organic substances contained in CP layers of *Pinctada vulgaris* show red fluorescence under the irradiation of a 404.7 nm line of mercury lamp. The organic substances contain porphyrin compound derivatives identified with the absorption bands. The distribution of red fluorescence inside CP layers shows lamellar pattern. This distribution follows CP layer lamellar arrangement and was supposedly formed during the shell growth process. The lamellar pattern of red fluorescence consists of red and black parallel zones. We found that red and black parallel zones are modulation of emission intensity corresponding to sulphur distribution. Extraction process using acid treatments and chromatographic column obtained extracted liquid containing porphyrin derivatives.

References

- [1]. Deheyn DD, Wilson NG (2011) Bioluminescent signals spatially amplified by wavelength-specific diffusion through the shell of a marine snail. In Proc R Soc B 278:2112-2121.
- [2]. Ohmiya Y, Kojima S, Nakamura M, Niwa H (2005) Bioluminescence in the *Limpet-Like Snail*, *Latia neritoides*. In Bull Chem Soc Jpn 78:1197-1205.
- [3]. Tan TL, Wong D, Lee P (2004) Iridescence of a shell of mollusk *Haliotis Glabra*. Opt Express 12:4847-4854.
- [4]. Brink DJ, van der Berg NG, Botha AJ (2002) Iridescence color of seashells: an optical and structural investigation of *Helcion pruinosus*. Appl Opt 41:717-721.
- [5]. Liu Y, Shigley JE, Hurwit KN (1999) Iridescence color of a shell of the mollusk *Pinctada Margaritifera* caused by diffraction. Opt Express 4:177-182.
- [6]. Wada K (1961) Crystal growth of molluscan shell. In Bull Natl Pearl Res Lab 7:703-828.
- [7]. Kobayashi I, Samata T (2006) Bivalve shell structure and organic matrix. Mater Sci Eng C 26:692-698.
- [8]. Farre B, Brunelle A, Laprevote O, Cuif JP, Williams CT, Dauphin Y (2011) Shell layers of the black-lip pearl oyster *Pinctada Margaritifera*: Matching microstructure and composition. Comp Biochem Physiol B 159:131-139.
- [9]. Iwahashi Y, Akamatsu S (1994) Porphyrin pigment in black-lip pearls and its application to pearl identification. Fish Sci 60:69-71.

- [10]. Miyoshi T, Matsuda Y, Komatsu H (1987) Fluorescence from pearl to distinguish mother oyster used in pearl culture. *Jpn J Appl Phys* 26:578-581.
- [11]. Comfort A (1951) The pigmentation of molluscan shell. *Biol Rev* 26:285-301.
- [12]. Comfort A (1950) Molluscan shell as a practical source of uroporphyrin I. *Science* 112:279-280.
- [13]. Zheng W, Shan N, Yu L, Wang X (2008) UV-visible, fluorescence and EPR properties of porphyrins and metalloporphyrins. *Dyes Pigments* 77:153-157.
- [14]. Dauphin Y, Brunelle A, Cotte M, Cuif JP, Farre B, Laprevote O, Meibom A, Salome M, Williams CT (2010) A layered structure in the organic envelopes of the prismatic layer of the shell of the pearl oyster *Pinctada margaritifera* (mollusca, bivalvia). *Microsc and Microanal* 16:91-98.
- [15]. Dauphin Y (2002) Comparison of the soluble matrices of the calcitic prismatic layer of *Pinna nobilis* (mollusca, bivalvia, Pteriomorpha). *Comp Biochem Physiol A* 132:577-590.
- [16]. Checa AG, Navarro ABR, Degado FJE (2005) The nature and formation of calcitic columnar prismatic shell layers in *Pterimorphian bivalves*. *Biomaterials* 26:6404-6414.
- [17]. Harper EM, Checa AG, Navarro ABR (2009) Organization and mode of secretion of the granular prismatic microstructure of *Entodesma navicula* (Bivalve: Mollusca). *Acta Zool.-Stockholm* 90:132-141.
- [18]. Comfort A (1949) The distribution of porphyrin fluorescence in molluscan shells, *Biochem J* 44:112-117.

- [19]. Gouterman M (1978) Optical spectra and electronic structure of porphyrins and related rings. in *The porphyrins*, III, D. Dolphin, Ed. (Academic Press, New York).
- [20]. Uttamlal M, Smith ASH (2008) The excitation wavelength dependent fluorescence of porphyrins. *Chem Phys Lett* 454:223-228.
- [21]. Lindsey JS, Chandrasher V, Taniguchi M, Ptaszek M (2011) Abiotic formation of uroporphyrinogen and coproporphyrinogen from acyclic reactants. *New J Chem* 35:65-75.
- [22]. Checa A (2000) A new model for periostacum and shell formation in Unionidae (bivalvia, Mollusca. *Tissue & Cell* 32:405-416.
- [23]. Nakahara H, Bevelander G (1971) The formation and growth of the prismatic layer of *Pinctada radiata*. *Calc Tiss Res* 7:31-45.
- [24]. Dauphin Y, Cuif JP, Doucet J, Salome M, Susini J, Williams CT (2003) In situ mapping of growth lines in the calcitic prismatic layers of mollusk shells using X-ray absorption near-edge structure (XANES) spectroscopy at the sulphur K-edge. *Mar Biol* 142:299-304.

Chapter 3

Rare Earth Recovery from Soda Lime Silicate

Glass Cullet by P₂O₅ Addition

3.1 Introduction

Rare earth elements are essential because they are widely utilized for developing high technology applications such as fuel cells, high capacity batteries, permanent magnet for wind power generation, etc. [1, 2]. They are also critical because their natural reserves are only concentrated in few countries and their supplies are strictly delimited. Moreover, they have hardly effective substitutes, low recycling rate, and unsustainable primary mining [3]. Intensive studies are being conducted to face this crucial situation including possibilities to recover rare earth elements from industrial waste residue, for example, red mud as a residue of smelting bauxite [4, 5], and glass-polishing sludge as a waste of glass industries [6, 7].

Spent glass-polishing slurry wasted from optical glass industries is of interesting industrial waste because its polishing sludge contains relatively high concentrated rare earth elements. The polishing sludge comprises Ce originated from polishing powder, glass

particles released from ground and polished glass surface, and alumina particles hydrolyzed from flocculants. The glass particles from ground and polished glass surfaces (i.e. LCD glass, optical glass, colorant in glass, etc.) might contain notable rare earth elements such as Yb, La, Gd, Er, Y, and Eu [8, 9]. Unfortunately, recycling of glass-polishing sludge only focuses on Ce recovery. In Ce recycling process, glass particles including other elements are discarded through chemical dissolution, filtration, or selective precipitation process [6–8, 10, 11]. As consequence, the valuable rare earth elements are wasted along with their hosts.

Therefore, after separating from Ce, glass particles containing rare earth elements need further processes. Common process to separate rare earth elements from glass host is hydrometallurgical process. However, these processes need large consumption of chemicals and releases harmful residues. For example, recovery of rare earth elements from spent optical glass used NaOH followed by HCl in leaching process [11]. Recovery of Ce from spent glass polishing powder used $\text{H}_2\text{C}_2\text{O}_4$ and H_2SO_4 [6], NaOH [7] and $\text{HNO}_3/\text{H}_2\text{O}_2$ mixture [8] to dissolve the powder. Most studies have tended to focus on efficient recovery of Ce while no one, to the best of our knowledge, has studied concerning recovery of rare earth element-containing glass particles in glass-polishing sludge with combination of pyrometallurgical and hydrometallurgical process without chemical treatments.

In this work, rare earth element-containing glass was melted with *monoammonium* phosphate ($\text{NH}_4\text{H}_2\text{PO}_4$) addition. *Monoammonium* phosphate was utilized to attract rare earth element from silicate to phosphate networks in glass host. By controlling phosphate composition, rare earth element in the glass can be leached into water. Initially, rare earth element was doped into glass cullet (soda-lime-silicate) to make simulated rare earth

element-containing glass particles. Then, the rare earth element-doped glass cullet was melted with a series of *monoammonium* phosphate concentrations then followed by leaching treatments. With phosphate addition, the glass cullet might be experimentally approached as a phospho-silicate glass system. Then, we exploited chemical behavior of phosphate in the matrix of silicate network: its high ionic field strength [12] to attract the rare earth element, its tendency of forming discrete anion complexes [13, 14] to cluster the rare earth element apart from silicate, and its low durability [15, 16] to leach phosphate with rare earth element using water. To study effect of phosphate addition to rare earth element, photoluminescence spectroscopy was employed to record emission spectra of rare earth element, especially if the glass samples show lack of transparency. Therefore, europium was selected as a dopant into glass cullet and its sensitive emission spectrum was utilized to estimate the local vicinity of europium ions whether it becomes in coordination with phosphate. Europium ions that coordinate with linear phosphate units are expected to occur within the series composition of phosphate. In that condition, solubility of rare earth element into water will enhance. Finally, europium was recovered from glass sample by leaching into water.

The objective of this study is to recover rare earth element from soda lime silicate glass cullet by utilizing phosphate. Photoluminescence were employed to obtain emission spectra, which are affected by surrounding structures. Then, inductively coupled plasma mass spectroscopy (ICP-MS) and fourier transform infrared (FTIR) spectroscopy were used to detect amount of europium elements dissolved in water, and phosphate structures of glass samples, respectively. This study introduces rare earth element-containing glass particle in

glass polishing sludge as a potential secondary resource of rare earth elements and offers recovery process without acid treatments.

3.2 Experimental Methods

We obtained soda lime silicate glass cullet from a glass company with chemical composition confirmed by SEM-EDX (JEOL JSM-6510 LV): 70.12SiO₂, 0.04Fe₂O₃, 1.06Al₂O₃, 14.34Na₂O, 0.51K₂O, 6.86MgO, 7.07CaO (mol %). Eu³⁺-doped glass cullet was made as simulated rare earth element-containing glass particle, and labelled as cullet+Eu. First, appropriate amount of glass cullet was ground in alumina mortar, thoroughly mixed with 1 mol % Eu₂O₃, and then melted using a platinum crucible in a high temperature electric furnace at 1500 °C in air atmosphere for about 2 hours, and followed by quenching in water for cooling to room temperature. Europium was selected because it has relatively simple energy levels [17], its ground ⁷F₀ and excited ⁵D₀ levels are non-degenerated, and its luminescence spectra show very sensitive to small changes in its local chemical vicinity. Through analyzing fluorescence emission spectra, we are able to estimate the changes in local chemical vicinity of Eu³⁺ ion due to monoammonium phosphate addition. It also allows us to measure small amount of sample either transparent or opaque conditions.

The addition of monoammonium phosphate is intended to attract rare earth utilizing high ionic field strength of phosphate [18–20], and simultaneously attract cations from silicate networks [21] such as Na⁺, K⁺, Ca²⁺, Mg²⁺. Sodium and potassium ions might lead to formation of linear phosphate chains, while calcium and magnesium ions can serve as ionic cross-links between two different linear phosphate chains. Cullet+Eu was reground and mixed with raw material of phosphate, NH₄H₂PO₄. This sample was labelled as (cullet+Eu)–

$x\text{P}_2\text{O}_5$, with x is the amount of P_2O_5 in mol %. For analyzing phosphate network chains or structures, it is also preferable to express the composition with molar ratio of alkali and alkaline earth metal oxides to phosphate, A/P-ratio [19]. The ratio shows a condition to form phosphate networks such as ultraphosphate (Q^3) cross-link network, metaphosphate (Q^2), pyrophosphate (Q^1), and orthophosphate (Q^0) as shown in Table 3.1.

$$\text{A/P-ratio} = \frac{\text{A}_2\text{O (mol \%)} + \text{A}'\text{O (mol \%)}}{\text{P}_2\text{O}_5 \text{ (mol \%)}} \quad (1)$$

where A is the alkali metal, and A' is the alkaline earth metal. x values are 15, 17, 22, 25, 30, 35, 40, 45 and corresponding A/P-ratio are 1.62, 1.39, 1.01, 0.85, 0.67, 0.53, 0.43, 0.34, respectively.

Table 3.1 Phosphate tetrahedral sites in phosphate glass [22] and A/P-ratio.

Ideal Composition (mol%):	100 P_2O_5	50 $\text{A}_2\text{O} - 50\text{P}_2\text{O}_5$	67 $\text{A}_2\text{O} - 33\text{P}_2\text{O}_5$	75 $\text{A}_2\text{O} - 25\text{P}_2\text{O}_5$
A/P-ratio :	0	1	2	3
PO_4 Tetrahedral Unit :				
$[\text{Q}^n]$:	Q^3	Q^2	Q^1	Q^0

: Bridging oxygen : Non-bridging oxygen A : Alkali ion n : number of bridging oxygen

Small amount of the admixture was melted at 1400–1500 °C in air atmosphere by employing single hot thermocouple technique [23], and subsequently quenched in air for cooling to room temperature. Two thermocouple wires (0.25 mm dia.) made of Pt and Pt-

13% Rh (R Type) were joined manually. The admixture was placed at the bend side of the joined wire. By regulating voltage supply, heat was supplied through thermocouple wire. Temperature of the wire gradually increased and heated the sample up to its melting temperature. After melting, voltage supply was stop quickly then the sample was normally quenched in air. A 0.01 gram of glass sample obtained from this technique takes about 3 minutes for cooling to room temperature. The accuracy of temperature measurements is estimated as $\pm 2-3$ °C. Using hot thermocouple technique enables us to control carefully voltage supply for slowly increasing temperature especially when $\text{NH}_4\text{H}_2\text{PO}_4$ started to decompose to NH_3 , P_2O_5 and H_2O at 180–250 °C. It also enables us to check visually when the sample started to melt and minimize melting time by holding it in melting condition for about 5 minutes.

In order to understand the local structure of (cullet+Eu) $-x\text{P}_2\text{O}_5$ system, it is necessary to understand the structure of simpler glass system from which the (cullet+ Eu) $-x\text{P}_2\text{O}_5$ system is derived. For that reason, several glasses system were prepared and doped with 1 mol % Eu_2O_3 using the same technique. They are silicate glasses 39.6 A_2O –59.4 SiO_2 (mol %), phosphate glasses, 49.5 A_2O –49.5 P_2O_5 (mol %), and phospho-silicate glasses, 9.9 A_2O –29.7 P_2O_5 –59.4 SiO_2 (mol %), with A is Li, Na, or K. Raw materials used to synthesize these glasses are reagent-grade of 99.9% Li_2CO_3 , 99.8% Na_2CO_3 , 99.5% K_2CO_3 , and 99.9% LiPO_3 , 99.9% NaPO_3 , 99.9 % KPO_3 , 99.9 % SiO_2 , and 99.0% $\text{NH}_4\text{H}_2\text{PO}_4$ and 99.9% Eu_2O_3 .

(Cullet+Eu) $-x\text{P}_2\text{O}_5$ with $x = 15, 22, 35,$ and 45 mol % were selected for leaching tests. The sample was placed in an alumina crucible, preheated at 180 °C for 22 hours in an electrical muffle furnace to decompose $\text{NH}_4\text{H}_2\text{PO}_4$ to NH_3 , H_2O and P_2O_5 . Then it was heated

up to a melting temperature of 1500 °C in air atmosphere using a platinum crucible for an hour in a high temperature electric furnace. After melting, these samples were quenched in water for cooling to room temperature.

To study effect of phosphate addition to rare earth element, absorption and transmittance spectroscopy technique can not be applied because the glass samples are opaque. Therefore, photoluminescence spectroscopy was employed to record emission spectra for estimating changes in local chemical vicinity of rare earth ions in glass system after introducing P₂O₅. Local chemical vicinity of Eu³⁺ ion affects symmetry of the ligand field Eu³⁺ ion and Eu-O covalency [24–26], and it may reveal to which network unit the rare earth ion coordinates with. Emission spectra of europium were analyzed especially ⁵D₀→⁷F₁ and ⁵D₀→⁷F₂ transition probabilities (Figure 3.1). The ⁵D₀→⁷F₁ and ⁵D₀→⁷F₂ are allowed magnetic dipole transition and forced electric dipole transition, respectively. The ⁵D₀→⁷F₁ transition is independent on matrix composition, while ⁵D₀→⁷F₂ is hypersensitive to the covalency and/or structural changes in the local chemical vicinity of the Eu³⁺ ion [24, 26]. The differences in Eu³⁺ emission spectra from each sample as a function of glass composition can be properly described by fluorescence intensity ratio, I-ratio as follows:

$$I - \text{ratio} = \frac{I (^5D_0 \rightarrow ^7F_2)}{I (^5D_0 \rightarrow ^7F_1)} \quad (2)$$

where I (⁵D₀ →⁷F₁) is the emission intensity of the ⁵D₀ →⁷F₁ transition, and I (⁵D₀ →⁷F₂) is the emission intensity of the ⁵D₀ →⁷F₂ transition. This ratio is widely used to estimate deviation from the symmetry of the ligand field of Eu³⁺ ion and Eu-O covalency [17, 25, 27–30]. Excitation and emission spectra of samples were recorded by photoluminescence

spectrometer (Hitachi, F-7000), working in the UV-visible range of 350–750 nm. It was operated at scanning speed 240 nm/min, slit width 2.5 nm with photomultiplier tube voltage of 400 volt. Emission spectra were measured under monitoring excitation wavelength 393 nm.

An infrared spectrophotometer (IR Prestige-21, Shimadzu) was used to observe IR spectra of glass samples. IR spectra provide information about local structure related to PO₄ and SiO₄ tetrahedral groups. The equipment was operated at room temperature in the range of 500–1600 cm⁻¹ by using the KBr disc technique. Transmission (%) of IR spectra was converted to Kubelka-Munk function intensity unit (arbitrary unit) with the correction of powder grain size.

Powdered samples (<150 μm) were leached using water (ultrapure water, pH 6.8–7.0) for 96 hours at room temperature. Concentration of rare earth dissolved into water was compared to initial concentration of rare earth in the sample to obtain recovery efficiency.

$$\% \text{ Recovery} = \frac{\text{Concentration of rare earth dissolved in water}}{\text{Initial concentration of rare earth in sample}} \times 100 \quad (3)$$

Initial concentrations of rare earth in the sample were obtained through acid digestion treatments using HF (38 wt %) and HNO₃ (68 wt %). Both are heated at 200 °C for 4 hours. Finally, the sample were leached using HNO₃ (3 wt %) for 48 hours at room temperature until it was completely dissolved in the solution. Inductively coupled plasma-mass spectroscopy (ICP-MS, Varian 820-MS) was used to determine concentration of the rare earth element dissolved in acid solution and water with an internal standard technique involving the addition of 2 mg/L of Re and Rh. A standard solution (Custom assurance

standard, Specx CertiPrep) containing 10 mg/L of rare earth elements including Eu was diluted from 0.15 to 0.0015 mg/L for composing precise linear line on calibration chart. R-square value obtained from that linear line is equal to 1.00.

3.3 Results and Discussion

3.3.1 Hypersensitive Emission Spectra to Estimate Local Vicinity of Eu^{3+} Ion

Photoluminescence was utilized to observe characteristic of excitation and emission spectra. Figure 3.1(a) shows excitation spectrum of Eu^{3+} -doped glass cullet with addition of phosphate (cullet+Eu)- $35\text{P}_2\text{O}_5$. There are six lines observed in the excitation spectrum. The most dominant line appeared at 393 nm. It ascribes to transition originating from the ${}^7\text{F}_0$ ground state to the ${}^5\text{L}_6$ excited states of Eu^{3+} . Under this excitation line, emission spectrum of Eu^{3+} was recorded as shown in Figure 3.1(b).

The emission spectrum presents transition bands arising from ${}^5\text{D}_0$ excited states to ${}^7\text{F}_J$ ($J = 0, 1, 2, 3$ and 4) ground states. Emission spectrum in ${}^5\text{D}_0 \rightarrow {}^7\text{F}_1$ transition of Eu^{3+} was observed at 593 nm, while the most intense line corresponded to ${}^5\text{D}_0 \rightarrow {}^7\text{F}_2$ transition was recorded at 614 nm. The band corresponded to ${}^5\text{D}_0 \rightarrow {}^7\text{F}_1$ transition presents a magnetic dipole nature and its fluorescence intensity is not affected by local chemical vicinity of Eu^{3+} ion, whereas ${}^5\text{D}_0 \rightarrow {}^7\text{F}_2$ transition is hypersensitive and is strongly dependent on the local chemical vicinity of Eu^{3+} ion. Therefore, fluorescence intensity of ${}^5\text{D}_0 \rightarrow {}^7\text{F}_1$ transition can be considered as a standard to compare the relative intensity of the other bands [25]. Fluorescence intensity ratio, I-ratios of ${}^5\text{D}_0 \rightarrow {}^7\text{F}_2$ to ${}^5\text{D}_0 \rightarrow {}^7\text{F}_1$ transition for silicate glasses, phosphate glasses, phospho-silicate glasses, and glass cullet, were calculated and listed in Table 3.2.

3.3.2 Fluorescence Intensity Ratio (I-ratio) of Simpler Glass System

To study the emission spectra of (cullet+Eu)- x P₂O₅ glass samples, it is necessary to analyze and compare to emission spectra of its simpler glass systems. If they show similar emission characteristics and corresponding I-ratio with those of simpler glass systems, that emission similarity indicates the same degree of their local chemical vicinity.

In Eu³⁺-doped silicate glasses, 39.6A₂O–59.4SiO₂ (mol %) (A = Li, Na, K), I-ratios vary upon the variation of modifier ions, and have a tendency to increase for larger ionic radius of modifier ions in the order of Li < Na < K (Table 3.2). The dependence of the I-ratio on the modifier ions results from a network modifier from alkali ion sat in the second neighboring ion of Eu³⁺ ion and located in a region of non-bridging oxygen of three-dimensional silicate network [20, 25]. This formation brings about large distortion in local chemical vicinity of Eu³⁺ ions when the network modifier ions are substituted in silicate glasses [27]. As a result, their I-ratios depend on composition with wide range from 3.01 to 3.79 (Table 3.2).

Unlike Eu³⁺-doped silicate glasses, I-ratios of Eu³⁺-doped metaphosphate glasses, 49.5A₂O–49.5P₂O₅ (mol %) (A = Li, Na, K) are compositional independence. The I-ratios slightly change upon the substitution of network modifiers. Metaphosphate glass is made up two-dimensional long chains by connecting PO₄ tetrahedral units through two bridging oxygen.

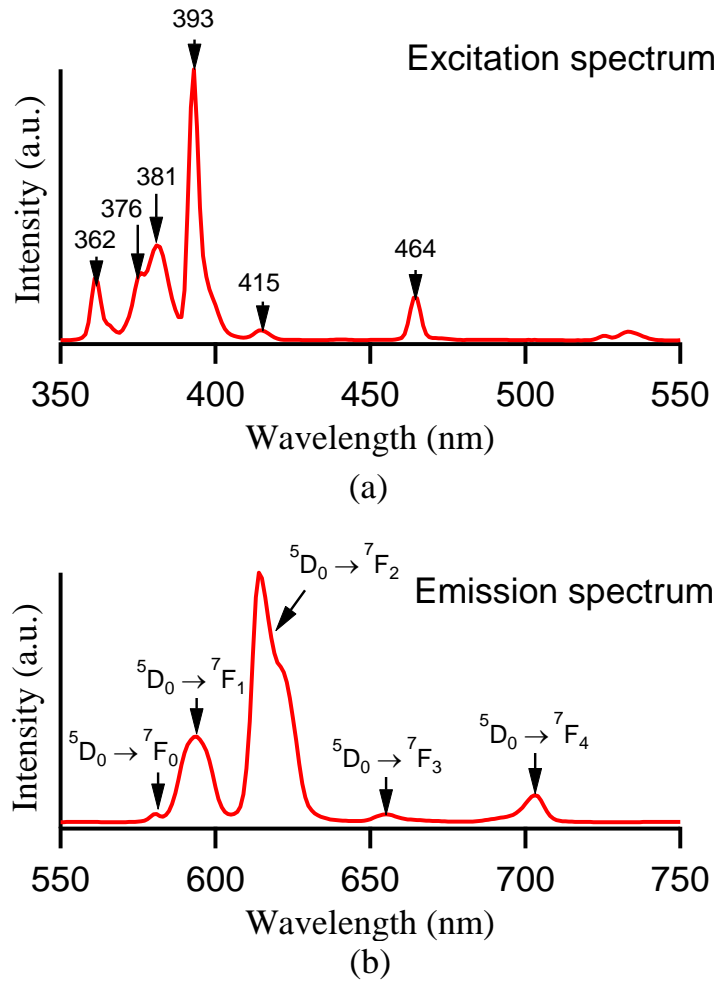


Figure 3.1 Spectra of (cullet+Eu)-35P₂O₅ glass sample (1 mol % Eu₂O₃, A/P-ratio = 0.53): (a) excitation spectrum with 614 nm monitored wavelength and (b) emission spectrum with 393 nm excitation wavelength.

Table 3.2 Fluorescence intensity ratio of ${}^5D_0 \rightarrow {}^7F_2$ to ${}^5D_0 \rightarrow {}^7F_1$ transition of Eu^{3+} in matrix glasses (silicate, phosphate, phospho-silicate and glass cullet) doped with 1 mol% Eu_2O_3 and quenched in air.

Matrix glass composition doped with Eu_2O_3 (mol%)	Emission peak (nm)		I-ratio** $I({}^5D_0 \rightarrow {}^7F_2) / I({}^5D_0 \rightarrow {}^7F_1)$
	${}^5D_0 \rightarrow {}^7F_1$	${}^5D_0 \rightarrow {}^7F_2$	
39.6Li ₂ O–59.4SiO ₂	593	615	3.01 ± 0.02
39.6Na ₂ O–59.4SiO ₂	594	613	3.62 ± 0.09
39.6K ₂ O–59.4SiO ₂	594	613	3.79 ± 0.08
49.5Li ₂ O–49.5P ₂ O ₅	593	615	2.54 ± 0.03
49.5Na ₂ O–49.5P ₂ O ₅	594	615	2.73 ± 0.03
49.5K ₂ O–49.5P ₂ O ₅	594	615	2.58 ± 0.02
9.9Li ₂ O–29.7P ₂ O ₅ –59.4SiO ₂	593	614	3.09 ± 0.02
9.9Na ₂ O–29.7P ₂ O ₅ –59.4SiO ₂	594	615	3.05 ± 0.02
9.9K ₂ O–29.7P ₂ O ₅ –59.4SiO ₂	594	614	3.14 ± 0.02
Glass cullet*	593	613	3.74 ± 0.02
(Cullet+Eu)–45P ₂ O ₅	593	614	3.00 ± 0.02

*Glass cullet composition: 69.42SiO₂–0.04Fe₂O₃–1.05Al₂O₃–14.19Na₂O–0.51K₂O–6.79MgO–7.07CaO (mol %).

** Average values of three measurements.

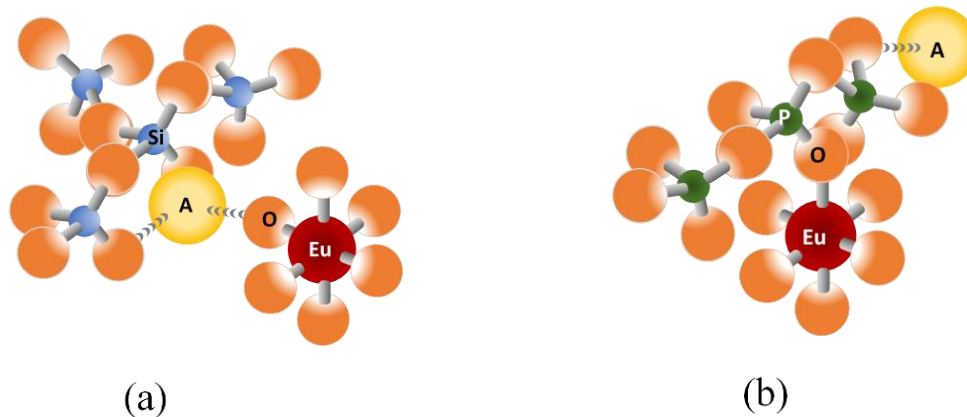


Figure 3.2 Illustration of local structure around Eu^{3+} ion in silicate and phosphate networks: (a) alkali earth or alkaline earth metal (symbolized as A) sits in the second neighbor of Eu^{3+} ion forming Eu-O-A linkage and (b) phosphorus sits in the second neighbor of Eu^{3+} ion forming Eu-O-P linkage.

The modifier ions occupy sites in between these chains, while the rare earth ions selectively coordinate with the P=O site (doubly bonded oxygen) [20]. Therefore, emission intensity at the ${}^5\text{D}_0 \rightarrow {}^7\text{F}_2$ transition of these glasses reflects small distortion in local chemical vicinity of Eu^{3+} ions with increasing ionic radius of alkali ions. As a result, I-ratios varied in narrow range of 2.54 to 2.73 (Table 3.2). Illustrations of Eu^{3+} ion linked to silicate and phosphate networks are shown in Figures 3.2(a) and 3.2(b).

In the phospho-silicate glass system, Eu^{3+} ion might coordinate with silicate networks or phosphate networks. Based on the result of the silicate and phosphate glasses, local chemical vicinity of Eu^{3+} ions will undergo large distortion when they are in coordination with silicate networks forming Eu-O-A as shown in Figure 3.2(a). Whereas only slight distortion occurs in local chemical vicinity of Eu^{3+} ions when they are in coordination with phosphate networks forming Eu-O-P as shown in Figure 3.2(b).

I-ratios of Eu^{3+} -doped phospho-silicate glasses $9.9\text{A}_2\text{O}-29.7\text{P}_2\text{O}_5-59.4\text{SiO}_2$ (mol %) (A = Li, Na, K) are nearly stable with narrow range of 3.05 to 3.14 (Table 3.2). This result shows that local chemical vicinity of Eu^{3+} ion in the phospho-silicate glasses did not experienced large distortion upon the variation of modifier ions. This indicates that the local chemical vicinities of Eu^{3+} ions in the phospho-silicate glasses are different from those of silicate glasses. Rather, local chemical vicinities of Eu^{3+} ions show similar tendency with those of phosphate glasses. This tendency most likely indicates that Eu^{3+} ions coordinate with PO_4 (Eu–O–P linkage) rather than SiO_4 tetrahedral unit. In addition, high ionic field strength of phosphate causes Eu^{3+} ions preferentially coordinate with phosphate networks. This result is in good agreement with a previous study dealing with selective coordination of Nd^{3+} with PO_4 tetrahedra in the system of $9.9\text{Na}_2\text{O}-29.7\text{P}_2\text{O}_5-59.4\text{SiO}_2$ (mol %) [19].

Even though containing multi components, Eu^{3+} -doped glass cullet has similar local chemical vicinity of Eu^{3+} ions with the simpler silicate glass, Eu^{3+} -doped $39.6\text{Na}_2\text{O}-59.4\text{SiO}_2$ (mol %) glass, because their I-ratios are nearly the same. Their emission intensities at the ${}^5\text{D}_0 \rightarrow {}^7\text{F}_2$ transition are in the same level (Figure 3.3(a)). Likewise, (cullet+Eu)- $45\text{P}_2\text{O}_5$ (mol %) content has also comparable I-ratios to the Eu^{3+} -doped $9.9\text{Na}_2\text{O}-29.7\text{P}_2\text{O}_5-59.4\text{SiO}_2$ (mol %) glass. Emission intensities at the ${}^5\text{D}_0 \rightarrow {}^7\text{F}_2$ transition of these glasses are also in the same level (Figure 3.3(b)).

3.3.3 Effect of Phosphate Addition upon I-ratio of Eu^{3+} -doped Glass Cullet

When a series concentration of phosphate, $x = 45, 40, 35, 30, 25, 22, 17, 15$ mol % corresponding to A/P-ratio = 0.34, 0.43, 0.53, 0.67, 0.85, 1.01, 1.39, 1.62, respectively, were introduced into the cullet+Eu system, I-ratios of those glasses system show a trend to level off until reach A/P-ratio = 1 (region A, Figure 3.4). In this condition, the I-ratios are comparable with that of Eu^{3+} -doped $9.9\text{Na}_2\text{O}-29.7\text{P}_2\text{O}_5-59.4\text{SiO}_2$ (mol %) glass, which indicates similar local chemical vicinity of Eu^{3+} ions. When A/P-ratio becomes higher than 1, I-ratios of those glasses system gradually increase to the range of silicate glasses (region B, Figure 3.4). On the basis of fluorescence intensity ratios from previous simpler glass samples (Table 3.2), it can be estimated that in the composition of A/P-ratio ≤ 1 , the amounts of P_2O_5 are sufficient to attract significant amounts of Eu^{3+} ions from silicate to phosphate networks. PO_4 tetrahedral units turn to dominate local chemical vicinity of almost all Eu^{3+} ions, and the local chemical vicinity is most likely the same as simpler phospho-silicate glass system. Thus, I-ratios in these compositions (A/P-ratio ≤ 1) are in the same range as simpler phospho-silicate glasses (Figure 3.4). Meanwhile, in the composition of A/P-ratio > 1 , less amounts of P_2O_5 are unable to attract amounts of Eu^{3+} ions. Most of the Eu^{3+} ions remain in coordinating with SiO_4 tetrahedral units, thus I-ratios increase to the range of silicate glasses with increasing A/P-ratio (Figure 3.4).

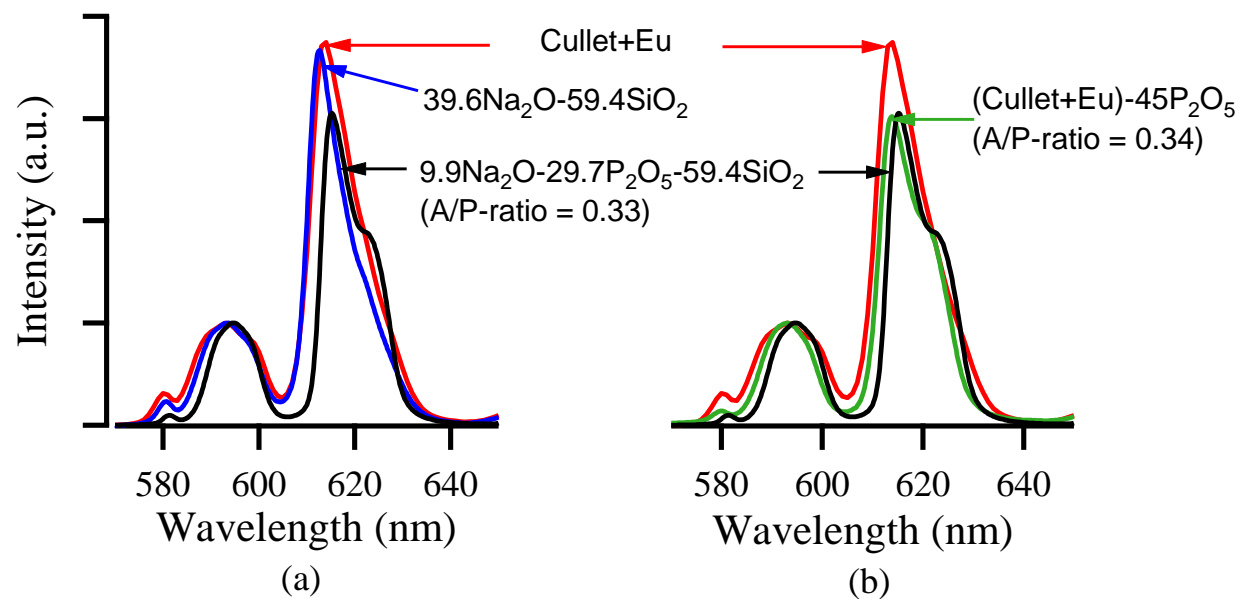


Figure 3.3 Emission spectra of Eu³⁺ in glass cullet, silicate and phospho-silicate glass matrices under 393 nm excitation: (a) emission intensity at ⁵D₀→⁷F₂ transition for glass cullet+Eu matrix is in comparison to silicate glass, (b) emission intensity at ⁵D₀→⁷F₂ transition for glass cullet+Eu with 45 mol % P₂O₅ addition, (cullet+Eu)-45P₂O₅, is in comparison to phospho-silicate glass matrix. The emission intensity of ⁵D₀→⁷F₁ transition has been normalized to a value of 1.0 to compare visually with that of ⁵D₀→⁷F₂ transition for investigated glasses.

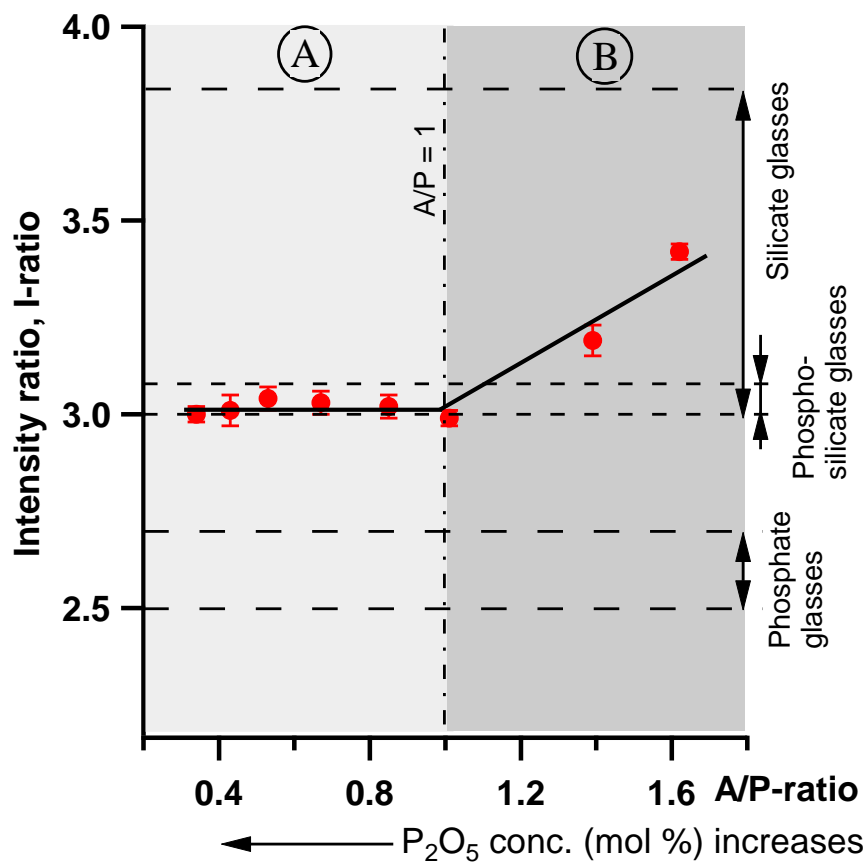


Figure 3.4 Fluorescence intensity ratio of (cullet+Eu)- x P₂O₅ (●) glass samples. Range of intensity ratio for silicate, phosphate, and phospho-silicate glasses from Table 3.2 are pointed by dash lines. Region A: sample composition with A/P-ratio ≤ 1 . Region B: sample composition with A/P-ratio > 1 . The solid line is guide to the eyes.

3.3.4 The Presence of Metaphosphate and Pyrophosphate Groups

FTIR spectroscopy was utilized to investigate local structure of samples related to PO_4 and SiO_4 groups. IR spectra are shown in Figure 3.5 with their assignments in Table 3.3. The addition of P_2O_5 into cullet+Eu glass has changed its silicate structure to phospho-silicate structure. In the IR spectra of (cullet+Eu)- $x\text{P}_2\text{O}_5$, large and intense bands in $900\text{--}1300\text{ cm}^{-1}$ (Figure 3.5) correspond to vibrations of Si-O-Si and P-O-P linkages [31-36]. IR spectrum for $x = 15\text{ mol \% P}_2\text{O}_5$ or A/P-ratio = 1.62 shows intense bands at $918, 1050,$ and 1123 cm^{-1} that are associated to stretching vibration of Si-O (Q^3), stretching vibration of Si-O-Si, and bending vibration of Si-O (Si-O-Si groups), respectively [31, 32]. Three narrow bands peaking at $622, 796,$ and 1199 cm^{-1} are assigned as cristobalite-like three-dimensional SiO_4 network [33, 34]. These silicate bands eventually weaken with increasing concentration of P_2O_5 addition (A/P-ratio < 1). On the other hand, weak bands observed in $1000\text{--}1100\text{ cm}^{-1}$ and $1200\text{--}1260\text{ cm}^{-1}$ become broad and intense bands with increasing concentration of P_2O_5 addition (A/P-ratio < 1). The bands in $1000\text{--}1100\text{ cm}^{-1}$ are associated to pyrophosphate groups (Q^1) [35, 36], and $1200\text{--}1260\text{ cm}^{-1}$ are assigned to asymmetric stretch of PO_2 bonds of metaphosphate groups (Q^2) [35, 37].

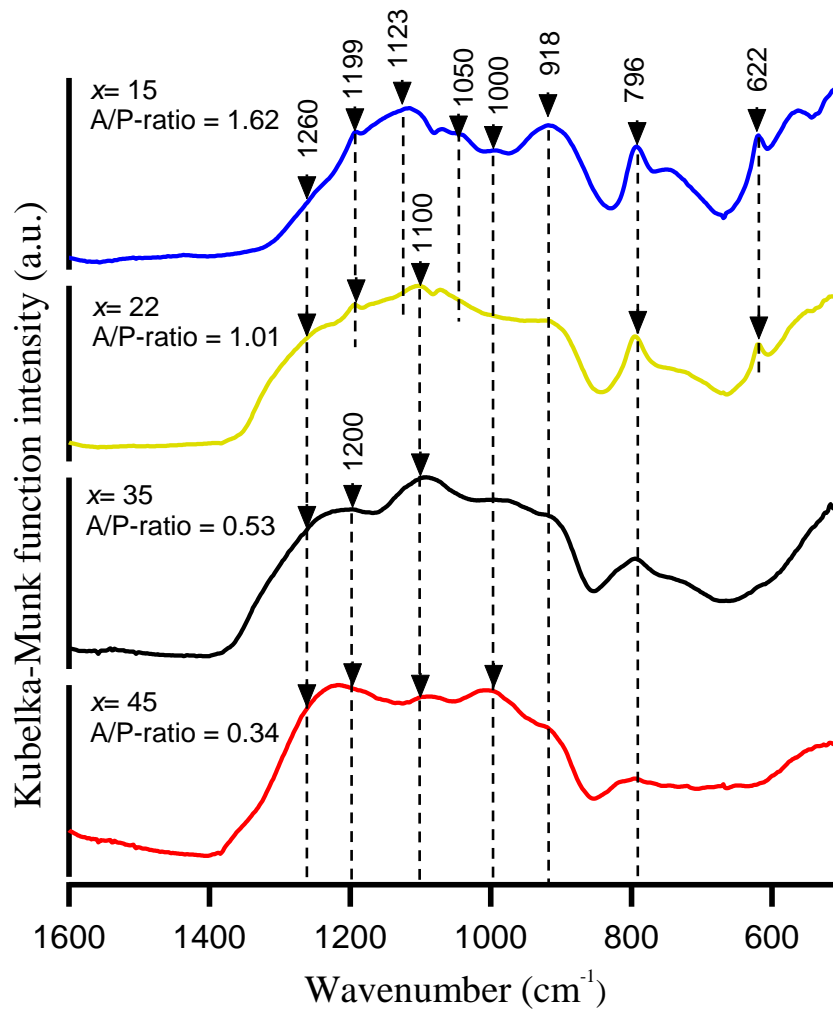


Figure 3.5 IR spectra of (cullet+Eu)- x P₂O₅ glass samples. The spectra indicate the presence of pyrophosphate (Q¹) and metaphosphate (Q²) groups. The assignments of absorption band are summarized in Table 3.3.

Table 3.3 IR band assignments in the range 500–1600 cm⁻¹ for (Cullet+Eu)_xP₂O₅ glass samples doped with 1 mol% Eu₂O₃ and quenched in water.

Wavenumber, cm ⁻¹	Assignments	References
622, 796, 1199	Cristobalite-like network	33, 34
790–800	Si–O–Si bending	31, 32
918–940	ν_s (Si–O), Q ³ groups	31, 32
1000–1100	ν_s (PO ₃) stretch, Q ¹ chain terminal	35, 36
1050	ν_s (Si–O–Si) stretch	31, 32
1100	ν_{as} (Si–O–P) stretch	35, 36
1123	ν_{as} (Si–O), Si–O–Si groups	31, 32
1200–1260	ν_{as} (PO ₂) stretch, Q ² units	35, 37

3.3.5 Recovery of Europium

Considering Eu³⁺ ions might selectively coordinate with PO₄ tetrahedral units in the composition of A/P-ratio ≤ 1 , glass samples were selected under this ratio for recovery process. Recovery of europium was conducted by leaching into water. Addition of P₂O₅ to recover europium elements shows positive result. Cullet+Eu without P₂O₅ ($x = 0$ mol %) recovered no europium element, while sample with 15 mol % P₂O₅ addition can recover 1% of total europium concentration (Region B, Figure 3.6). Recovery of europium became more efficient with increasing concentration of P₂O₅ addition. In region A where A/P-ratio ≤ 1 , recovery efficiency has exceeded 50%, and increased to 97% and reached 100% with 22, 35, and 45 mol % P₂O₅ addition, respectively.

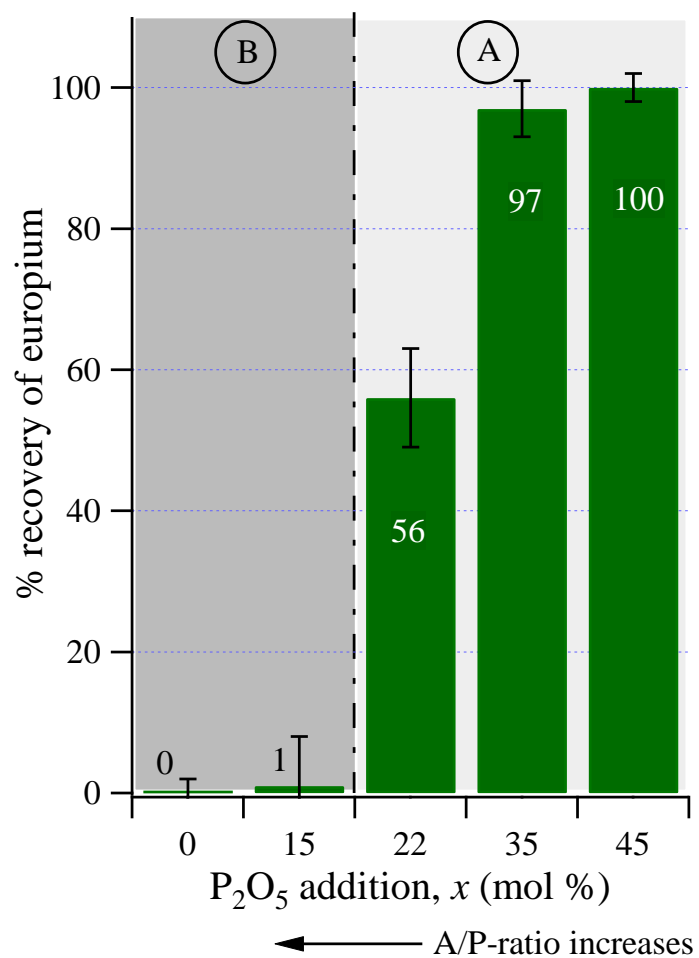


Figure 3.6 Recovery efficiency of Eu^{3+} dissolved in water in different compositions. Region A: sample composition with A/P- ratio ≤ 1 . Region B: sample composition A/P- ratio > 1 , also shown in Figure 3.4.

3.3.6 Recovery of Eu^{3+} Increases with the Presence of Metaphosphate Chains

Low recovery efficiency indicates that addition of P_2O_5 with concentration lower than those of alkali and alkaline earth metals are unable to attract significant amount of Eu^{3+} ions from SiO_4 units due to lack of PO_4 units forming pyrophosphate and metaphosphate groups (Region B). In this condition, I-ratios also show that SiO_4 tend to affect the vicinity of Eu^{3+} indicating that Eu^{3+} ions remain in coordinating with SiO_4 tetrahedral units. In addition, local structures are dominated by silicate networks indicated by the presence of Si–O–Si vibration and cristobalite-like linkages that have inherently good durability in water [38, 39].

In region A with A/P-ratio ≤ 1 , the concentrations of P_2O_5 are similar to and higher than those of alkali metals and alkaline earth metals. In this condition, metaphosphate chains started to grow with increasing concentration of P_2O_5 and coordinated with significant amount of Eu^{3+} ions as can be estimated from the I-ratio. Because metaphosphate chains have weak durability in aqueous solutions [40], recovery efficiency of Eu^{3+} ions into water reaches more than 50% (Region A, Figure 3.6). When A/P-ratio = 0.34, metaphosphate chains dominated the phospho-silicate structures, recovery efficiency achieved 100%.

3.4 Conclusion

The rare earth element was successfully recovered from simulated glass particles. Eu^{3+} ions were likely to coordinate selectively with PO_4 tetrahedral units rather than SiO_4 tetrahedral units upon the addition of P_2O_5 in the simulated glass. When concentration of P_2O_5 is similar to and higher than those of alkali and alkaline earth metals in glasses (A/P-ratio ≤ 1), PO_4 tetrahedral units in metaphosphate chains attract significant amounts of Eu^{3+}

ions. As consequence, 50–100% of europium is recovered. This recovery efficiency might be promoted by solubility of metaphosphate (Q^2) chains that started to exist in the local structure of glass sample in the composition with A/P-ratio ≤ 1 . This study offers recovery process for rare earth contained in glass host such as glass particles in glass-polishing sludge. P_2O_5 addition and water leaching can be a promising process to recover rare earth elements from glass-polishing sludge. This research contributes to the sustainability of rare earth elements. Further studies need to be conducted before applying this process in industrial application such as increasing recovery efficiency while reducing the amounts of P_2O_5 addition. Since raw material of phosphate is finite resource, we also consider in our further research to recycle phosphate from the leaching solution in sustainable recycling systems.

References

- [1] McLellan BC, Corder GD, Ali SH (2013) Sustainability of rare earths – An overview of the state of knowledge. *Minerals* 3:304–317.
- [2] Ronda CR, Jüstel T, Nikol H (1998) Rare earth phosphors: fundamentals and applications. *J Alloys Compd* 275-277:669–676.
- [3] Massari S, Ruberti M (2013) Rare earth elements as critical raw materials: Focus on international markets and future strategies. *Resour Policy* 38:36–43.
- [4] Borra CR, Blanpain B, Pontikes Y, Binnemans K, Van Gerven T (2015) Smelting of bauxite residue (red mud) in view of iron and selective rare earth recovery. *J Sustain Metall.*
- [5] Ochsenkühn-Petropulu M, Lyberopulu T, Ochsenkühn KM, Parissakis G (1996) Recovery of lanthanides and yttrium from red mud by selective leaching. *Anal Chim Acta* 319:249–254.
- [6] Kim JY, Kim US, Byeon MS, Kang WK, Hwang KT, Cho WS (2011) Recovery of cerium from glass polishing slurry. *J Rare Earths* 29:1075–1078.
- [7] Kato K, Yoshioka T, Okuwaki A (2000) Study for recycling of ceria-based glass polishing powder. *Ind Eng Chem Res* 39:943-947.
- [8] Jiang Y, Shibayama A, Liu K, Fujita T (2005) A hydrometallurgical process for extraction of lanthanum, yttrium and gadolinium from spent optical glass. *Hydrometallurgy* 76:1–9.

- [9] Liu Z, Qi C, Dai S, Jiang Y, Hu L (2003) Spectra and laser properties of Er³⁺, Yb³⁺: phosphate glasses. *Opt Mater* 21:789–794.
- [10] Xu T, Peng H (2009) Formation cause, composition analysis and comprehensive utilization of rare earth solid wastes. *J Rare Earths* 27:1096–1102.
- [11] Binnemans K, Jones PT, Blanpain B, Van Gerven T, Yang Y, Walton A, Buchert M (2013) Recycling of rare earths: a critical review. *J Clean Prod* 51:1–22.
- [12] Mirsaneh M, Reaney IM, Hatton PV, Bhakta S, James PF (2008) Effect of P₂O₅ on the early stage crystallization of K-fluorrichterite glass-ceramics. *J Non Cryst Solids* 354:3362–3368.
- [13] Liu SJ, Zhang YF, He W, Yue YZ (2011) Transparent phosphosilicate glasses containing crystals formed during cooling of melts. *J Non Cryst Solids* 357:3897–3900.
- [14] Oliveira JM, Correia RN, Fernandes MH (2000) Effect of SiO₂ on amorphous phase separation of CaO–P₂O₅–SiO₂–MgO glasses. *J Non Cryst Solids* 273:59–63.
- [15] O’Donnell MD, Watts SJ, Law RV, Hill RG (2008) Effect of P₂O₅ content in two series of soda lime phosphosilicate glasses on structure and properties - Part I: NMR. *J Non Cryst Solids* 354:3554–3560.
- [16] Cha J, Kubo T, Takebe H, Kuwabara M (2008) Compositional dependence of properties of SnO–P₂O₅ glasses. *J Ceram Soc Japan* 116:915–919.
- [17] Capobianco JA, Proulx PP, Bettinelli M, Negrisolo F (1990) Absorption and emission spectroscopy of Eu³⁺ in metaphosphate glasses. *Phys Rev B* 42:5936–5944.

- [18] Elwert T, Goldmann D, Schirmer T, Strauß K (2014). Affinity of rare earth elements to silico-phosphate phases in the system $\text{Al}_2\text{O}_3\text{-CaO-MgO-P}_2\text{O}_5\text{-SiO}_2$. *Chemie Ing Tech* 86:840–847.
- [19] Nakamura H, Saitoh A, Takebe H (2013) Composition condition of phosphosilicate glasses for rare-earth concentration. *J MMIJ* 129:591–595 (in Japanese).
- [20] Murata T, Moriyama Y, Morinaga K (2000) Relationship between the local structure and spontaneous emission probability of Er^{3+} in silicate, borate, and phosphate glasses. *Sci Technol Adv Mater* 1:139–145.
- [21] Li D, Fleet ME, Bancroft GM, Kasrai M, Pan Y (1995) Local structure of Si and P in $\text{SiO}_2\text{-P}_2\text{O}_5$ and $\text{Na}_2\text{O-SiO}_2\text{-P}_2\text{O}_5$ glasses: a XANES study. *J Non Cryst Solids* 188:181–189.
- [22] Brow RK. (2000) Review: the structure of simple phosphate glasses. *J Non Cryst Solids* 263&264:1-28.
- [23] Ohta Y, Morinaga K, Yanagase T (1980) Application of hot-thermocouple to high temperature chemistry. *Bull Japan Inst Met* 19:239–245.
- [24] Reisfeld R, Lieblich N (1973) Optical spectra and relaxation of Eu^{+3} in germanate glasses. *J Phys Chem Solids* 34:1467–1476.
- [25] Oomen EWJL, Van Dongen AMA (1989) Europium (III) in oxide glasses – Dependence of the emission spectrum upon glass composition. *J Non Cryst Solids* 111:205–213.
- [26] Velapoldi RA, Reisfeld R, Boehm L (1973) Quantum efficiencies and transition probabilities of Eu^{3+} in silicate glasses. *Phys Chem Glass* 14:101–106.

- [27] Nageno Y, Takebe H, Morinaga K, Izumitani T (1994) Effect of modifier ions on fluorescence and absorption of Eu^{3+} in alkali and alkaline earth silicate glasses. *J Non Cryst Solids* 169:288–294.
- [28] Dejneka M, Snitzer E, Riman RE (1995) Blue, green and red fluorescence and energy transfer of Eu^{3+} in fluoride glasses. *J Lumin* 65:227–245.
- [29] Avila LR, Nassor ECDO, Pereira PFS, Cestari A, Ciuffi KJ, Calefi PS, Nassar EJ (2008) Preparation and properties of europium-doped phosphosilicate glasses obtained by the sol-gel method. *J Non Cryst Solids* 354:4806–4810.
- [30] Elisa M, Sava BA, Vasiliu IC, Monteiro RCC, Veiga JP, Ghervase L, Feraru I, Iordanescu R (2013) Optical and structural characterization of samarium and europium-doped phosphate glasses. *J Non Cryst Solids* 369:55–60.
- [31] Serra J, González P, Liste S, Serra C, Chiussi S, León B, Pérez-Amor M, Ylänen HO, Hupa M (2003) FTIR and XPS studies of bioactive silica based glasses. *J Non Cryst Solids* 332:20–27.
- [32] Chimalawong P, Kaewkhao J, Limsuwan P (2012) Spectroscopic studies of Nd^{3+} doped soda-lime-silicate glasses. *J Mater Sci Eng B* 2:363–367.
- [33] Handke M, Sitarz M, Rokit M, Galuskin E (2003) Vibrational spectra of phosphate-silicate biomaterials. *J Mol Struct* 651-653:39–54.
- [34] Sitarz M, Fojud Z, Olejniczak Z (2009) The aluminium effect on the structure of silico-phosphate glasses studied by NMR and FTIR. *J Mol Struct* 924-926:107–110.
- [35] Lai YM, Liang XF, Yang SY, Wang JX, Cao LH, Dai B (2011) Raman and FTIR spectra of iron phosphate glasses containing cerium. *J Mol Struct* 992:84–88.

- [36] Moustafa YM, El-Egili, K (1998) Infrared spectra of sodium phosphate glasses. *J Non Cryst Solids* 240:144–153.
- [37] Ahsan MR, Mortuza MG (2005) Infrared spectra of $x\text{CaO}(1-x-z)\text{SiO}_2z\text{P}_2\text{O}_5$ glasses. *J Non Cryst Solids* 351:2333–2340.
- [38] Doremus RH, Mehrotra Y, Lanford WA, Burman C (1983) Reaction of water with glass: influence of a transformed surface layer. *J Mater Sci* 18:612–622.
- [39] Paul A (1977) Chemical durability of glasses; a thermodynamic approach. *J Mater Sci* 12:2246–2268.
- [40] Bunker BC, Arnold GW, Wilder JA (1984) Phosphate glass dissolution in aqueous solutions. *J Non Cryst Solids* 64:291–316. doi:10.1016/0022-3093(84)90184-4.

Chapter 4

General Conclusion

In this thesis, industrial wastes namely shell waste and glass-polishing sludge were investigated to acknowledge their potential values that can be recovered and recycled. Characterization of the wastes would enable them to be valorized towards functional materials.

Chapter 1 reviews pearl oyster farming process and production process of glass, and the waste generated from that processes. It also presents potential values of the waste and some issues in particular dealing with recycling processes of rare earth elements. The main objectives of this thesis are characterization of shell waste, *Pinctada vulgaris* from pearl oyster farming and recovery of rare earth elements from glass-polishing sludge.

Chapter 2 describes optical characterization of fluorescent matter from wasted shell of *Pinctada vulgaris* shells. Fluorescent matter occupies at the outer part of the shell, namely prismatic layers. Microstructure of prismatic layers is dominated by calcite (CaCO_3) with vertical organic membranes and growth lines transecting the organic membranes. Organic substances are present in prismatic layers as appear in weight loss and exothermic reactions

of TG-DTA curve of powdered prismatic layers. The fluorescent matter might be originated from these organic substances and it forms black-red lamellar pattern under UV irradiation in the cross section of prismatic layers. Observation using fluorescence microspectroscopy revealed that the black-red fluorescent lamellar pattern is due to emission intensity modulation and correspond to sulphur element concentration. The fluorescent matter both in prismatic layers and in extracted liquid is originated from porphyrin derivatives-containing organic substance.

Further investigations are necessary to explore deeply about the fluorescent matter distribution in prismatic layers. The lamellar fluorescence distribution might be an indication of certain condition of the pearl oyster during growth period, for example, sea environment and climate change, metabolism of the pearl oyster and quality level of the pearl in the shell.

Chapter 3 presents the effect of phosphate addition on recovery of rare earth elements from glass particles-containing glass-polishing sludge. Recovery of rare earth element from glass particles-containing glass-polishing sludge was conducted by melting with *monoammonium* phosphate ($\text{NH}_4\text{H}_2\text{PO}_4$) addition and then leaching into water. Glass cullet doped with rare earth was used as simulated glass particles because it has multi-components. By melting with P_2O_5 , however, glass samples became lack of transparency. For that reason, europium was selected as dopant in glass cullet and utilized its fluorescence spectra for the estimation of local structure around europium ions. Fluorescence intensity ratio of Eu^{3+} , I-ratio was calculated to estimate local vicinity of Eu^{3+} ions, whether Eu-O-A or Eu-O-P coordination. Addition of P_2O_5 to the glass cullet system changed glass structure from silicate networks to phospho-silicate networks. When phosphate was added into the glass cullet,

phosphate with the alkali-alkaline earth metals in glass cullet would form PO₄ networks: orthophosphate, pyrophosphate, and/or metaphosphate. The effect of P₂O₅ addition to I-ratio of (cullet+Eu)-*x*P₂O₅ glass was found in two conditions: A/P ratio > 1 and A/P ratio ≤ 1. I-ratio of (cullet+Eu)-*x*P₂O₅ glasses in the condition A/P ratio > 1 are comparable to the simple silicate glass system. Meanwhile, I-ratios of (cullet+Eu)-*x*P₂O₅ glasses in the condition A/P ratio ≤ 1 most likely indicate the formation of Eu–O–P coordination. IR spectra of (cullet+Eu)-*x*P₂O₅ glasses indicate the presence of metaphosphate (Q²) chains at A/P ratio ≤ 1 such as (cullet+Eu)-45P₂O₅. The presence of the metaphosphate chains increases with increasing phosphate content indicated by increasing absorption intensity (1200–1260 cm⁻¹). Since metaphosphate chains and Eu–O–P coordination are present in the same condition, A/P ratio ≤ 1, it is estimated that metaphosphate chains coordinate with significant amounts of Eu³⁺ ions. The metaphosphate chains in the condition of A/P ratio ≤ 1 might promote recovery efficiency of europium due to their weak durability in aqueous solutions. Therefore, by controlling A/P ratio ≤ 1, optimum condition can be obtained to recover rare earth elements from glass-polishing sludge with high efficiency.

In conclusion, I believe that these findings will contribute to the internal recycling process of pearl oyster farming companies and glass industries as well as the development of waste recycling technology inter-industries. In addition, the development of these findings should be supported by further intensive investigations to provide and demonstrate best practice and progress of converting the industrial wastes towards functional materials.